DESIGN AND EVALUATION OF AN ELEVATED TEMPERATURE CUTTING FORCE DYNAMOMETER FOR HYBRID MANUFACTURING

A Dissertation Presented for the
Doctor of Philosophy
Degree
The University of Tennessee, Knoxville

Justin Lucas West
December 2023

Copyright

Notice: This manuscript has been authored by UT-Battelle, LLC, under contract DE-AC05-00OR22725 with the US Department of Energy (DOE). The US government retains and the publisher, by accepting the article for publication, acknowledges that the US government retains a nonexclusive, paid-up, irrevocable, worldwide license to publish or reproduce the published form of this manuscript, or allow others to do so, for US government purposes. DOE will provide public access to these results of federally sponsored research in accordance with the DOE Public Access Plan (http://energy.gov/downloads/doe-public-access-plan).

Acknowledgments

This work would not have been possible without the support of:

Dr. Tony Schmitz and the Machine Tool Research Center
Dr. Scott Smith, Dr. Chris Tyler, Emma Betters, and many other great staff members at the Manufacturing Demonstration Facility at Oak Ridge National Laboratory
The Industrial Base Analysis and Sustainment (IBAS) program

Abstract

Cutting force coefficients, workpiece dynamics, and uncut chip area all change as a function of temperature during machining processes at elevated temperatures. In a traditional milling process, these parameters are nearly constant. The bulk workpiece temperature remains well below the working limit of the material, generally near room temperature. However, workpiece temperatures in hybrid manufacturing, where additive deposition precedes machining, are spatially and temporally variable. A milling force model that does not incorporate temperature effects will generally overestimate the cutting force and workpiece dynamic stiffness and underestimate the chip area. Milling parameters that are stable at room temperature may be unstable at higher temperatures, leading to unexpected chatter and poor part quality.

A cutting force dynamometer was designed, constructed, and tested to measure cutting force during milling with the workpiece heated to a constant bulk temperature of up to 500°C. The measured cutting forces were used to determine temperature dependent cutting force coefficients. These coefficients and workpiece dynamics were integrated into a time domain milling simulation to predict cutting force and stability under elevated temperature conditions. The outcome is improved modeling capabilities for hybrid manufacturing processes.

Keywords: cutting force, hybrid manufacturing, metrology, thermally assisted machining

Table of Contents

1 Introduction **1**

2 Literature Review **5**

2.1 Machining dynamics 6

2.2 Thermally enhanced machining 18

2.3 Hybrid manufacturing 27

3 Materials and Methods **34**

3.1 Dynamometer design 35

3.1.1 Constrained motion dynamometer 36

3.1.2 Thermal protection system 45

3.2 Measurement 59

3.2.1 Materials and equipment 59

3.2.2 Experimental procedure 63

3.2.3 Data processing 67

4 Results and Discussion **72**

4.1 Elevated temperature force dynamometer 72

4.2 Cutting force results 82

4.3 Milling time domain simulation 95

5 Conclusion **105**

References **106**

Vita **114**

List of Tables

2.1 Summary of cutting force results for thermally enhanced machining . 25
2.2 Summary of cutting tool material properties 28

3.1 Constrained motion dynamometer geometry. 39
3.2 Select material properties 48
3.3 Unit cell names 52
3.4 Select simulation results for Inconel lattices. 54
3.5 Instrumentation and associated measurement uncertainty. 60
3.6 Summary of cutting parameters. 65
3.7 Summary of cutting tests, completed in both the X and Y directions. 66

4.1 Workpiece temperature standard deviation from steady state mean. . 76
4.2 Temperature combined measurement uncertainty. 76
4.3 Average and standard deviation of capacitance gauge noise with convective cooling. 79
4.4 Average and standard deviation of natural frequency and modal stiffness at nominal workpiece temperatures. Four measurements were taken at each temperature. 81
4.5 Average of the peak cutting force. 88
4.6 Average of the mean cutting force. 88
4.7 Cutting force coefficients with temperature. 99
4.8 Simulated average of the Y peak cutting force. 99

List of Figures

2.1 Unstable simulation results for force (top) and displacement (bottom) 8
2.2 Chip thickness variation 8
2.3 Example single degree of freedom FRF. 10
2.4 Example multiple degree of freedom FRF. 10
2.5 Milling chip thickness 12
2.6 Example time domain 25% radial immersion down milling cutting force components 12
2.7 Exit and start angle geometry for up and down milling. 15
2.8 Example analytic stability map 16
2.9 Cutting tests for coefficient linear regression. 16
2.10 Example simulated stability map 17
2.11 Laser assisted turning 19
2.12 Simulated temperature distribution for laser assisted machining of Ti-6Al-4V 21
2.13 Challenges in integrating laser assisted machining (LAM) into a milling process. The red square shows that a fixed location heat source is not adequate for milling operations in different directions. 22
2.14 Laser assisted milling with integrated optics 23
2.15 Ti-6Al-4V tool wear for traditional milling and laser assisted milling . 26
2.16 Tool wear in Monel 400, Vc is surface speed in m/min 26
2.17 Stability limit dependence on temperature, 7075 29
2.18 Thermographic analysis of WAAM steel 31

2.19 Process diagram of iterative additive manufacturing. 33

3.1 Constrained motion dynamometer (CMD) impact testing and components. 37
3.2 Constrained motion dynamometer (CMD) geometry. Dimensions are provided in Table 3.1. 39
3.3 Natural frequency vs. temperature for a fixed free beam, see Equation 3.4 41
3.4 Change in FRF with flexure platform temperature. 42
3.5 Filtered displacement data for a cut that becomes unstable at elevated temperature with constant cutting parameters. 43
3.6 Simulated stability lobe diagram. Blue is at 20°C, red is at 300°C. . . 44
3.7 Comparison of FRF with (left) and without (right) a rigid calcium silicate insulator. Y is flexible (long) direction, and X the stiff (short) direction. 46
3.8 Grid of unit cells 51
3.9 Modeled re-entrant lattice structure. 52
3.10 Example lattice stiffness conductivity simulation, boundary conditions shown. 53
3.11 Example lattice thermal conductivity simulation, boundary conditions shown. 53
3.12 As printed Inconel lattice structure. 56
3.13 Elevated temperature cutting force dynamometer. 57
3.14 Elevated temperature cutting force dynamometer assembly. 58
3.15 Measurement setup 61
3.16 Infrared thermal image calibrated with thermocouple. 62
3.17 Cutting test at 400°C in Ti-6Al-4V. 65
3.18 Selection of cutting data. Blue is the trimmed displacement data, colored selections represent different feed rates. 69
3.19 Overlaid displacement data for one set of cutting tests, five feed rates. 69
3.20 Peak picking of measured FRF. 70

3.21 single degree of freedom (SDOF) frequency response function (FRF) measurement and fit 71
3.22 (Top) Inverse FRF and filtered inverse FRF. (Bottom) filter. 71

4.1 Spectral emissivity of various materials 74
4.2 Calibrated IR image of 500°C cutting test. 75
4.3 Temperature of the dynamometer platform, workpiece, and insulator up to a workpiece temperature of 500°C. 75
4.4 Testing the effect of the air cooling on the temperature of the dynamometer platform, workpiece, and insulator up to a workpiece temperature of 400°C. 78
4.5 Frequency response of the constrained motion dynamometer with changing workpiece temperature over one set of cutting tests. 79
4.6 Plot of all measured and fitted dynamometer FRFs, four sets of tests at six temperatures. 80
4.7 Workpiece cooled to room temperature after elevated temperature cutting. The staircase effect seen at the top of the workpiece and identified by the arrow is the result of thermal expansion. 81
4.8 Y cutting force at 20°C and 150$\frac{\mu m}{tooth}$. All tooth impacts are overlaid. . 83
4.9 X cutting force at 20°C and 150$\frac{\mu m}{tooth}$. All tooth impacts are overlaid. . 84
4.10 X cutting force at 100$\frac{\mu m}{tooth}$ over six temperatures. 85
4.11 Y cutting force at 100$\frac{\mu m}{tooth}$ over six temperatures. 86
4.12 X direction forces with constant feed and free cooling. 87
4.13 Peak force in X over a range of temperatures and feed rates in Ti-6Al-4V. 89
4.14 Mean force in X over a range of temperatures and feed rates in Ti-6Al-4V. 90
4.15 Peak force in Y over a range of temperatures and feed rates in Ti-6Al-4V. 91
4.16 Mean force in Y over a range of temperatures and feed rates in Ti-6Al-4V. 92
4.17 Peak resultant force over a range of temperatures and feed rates in Ti-6Al-4V. 93
4.18 Chip welding at 500°C, conventional milling. 94

4.19 Linear fit of cutting force vs. feed rate for Y direction over all temperatures. 98
4.20 Linear fit of cutting force vs. feed rate for X direction directions over all temperatures. 100
4.21 Cutting for coefficients with temperature. 101
4.22 Measured and simulated X force at 20°C and $100\frac{\mu m}{tooth}$. 101
4.23 Measured and simulated Y force at 20°C and $100\frac{\mu m}{tooth}$. 102
4.24 Measured and simulated X force at 500°C and $100\frac{\mu m}{tooth}$. 103
4.25 Measured and simulated Y force at 500°C and $100\frac{\mu m}{tooth}$. 104

Acronyms

ADOC axial depth of cut.

AM additive manufacturing.

CMD constrained motion dynamometer.

CNC computer numerical control.

DAQ data acquisition.

DED directed energy deposition.

EDM electrical discharge machining.

FFT fast Fourier transform.

FRF frequency response function.

HRSA heat resistant super alloys.

IIR infinite impulse response.

IR infrared.

LAM laser assisted machining.

MRR metal removal rate.

PID proportional-integral-derivative.

R&D research and development.

RDOC radial depth of cut.

RTD resistance temperature detector.

SDOF single degree of freedom.

SLE special limits of error.

TEM thermally enhanced machining.

Nomenclature

X	measured displacement
β	angle between the normal and resultant force
$\frac{X}{F}$	receptance
Ω	spindle speed
ω	frequency
ϕ_e	exit angle
ϕ_s	start angle
A	cross sectional area
a	radial depth of cut
b	axial depth of cut
E	modulus of elasticity
F	mean cutting force
f	linear feed
f_n	natural frequency
f_t	feed per tooth
h	time dependent chip thickness

I second moment of area

k_n component stiffness

k_n normal cutting force coefficient

K_s specific cutting force

k_t tangential cutting force coefficient

k_{beam} fixed-free beam stiffness

$k_{compressive}$ compressive stiffness

k_{eq} equivalent stiffness

L length

m mass

N_t number of cutter teeth

r tool radius

t thickness

Chapter 1

Introduction

Over the past four decades, the use of additive manufacturing (AM) has increased exponentially as new technologies have been developed to improve part quality, increase part complexity, and expand the selection of materials [1]. These advances have facilitated a shift from AM being used primarily for rapid prototyping to a method for final part production. The range of materials has expanded from thermoplastics to fibers, concrete, thermoset plastics, living tissue, and nearly every weldable alloy. According to a 2014 Wohlers Report, 29% of parts built on AM systems are used as functional parts. In 2019 they reported the metal material segment of the 3D printing industry had grown at 40% annually from 2014-2018, indicating an increasing use of AM for production applications [2]. Porsche, Sandvik, and Boeing have developed printed pistons, face mills, helicopter main rotor systems, respectively [3, 4, 5]. This challenging shift from prototype to production is at the center of manufacturing research and development (R&D) laboratories around the world. Production parts must meet higher functional, cost, and volume requirements. Currently, AM processes are typically unable to achieve geometric and finish tolerances for industries such as aerospace, automotive, and defense. As a result, many components produced with AM are better classified as near net shape preforms that require some degree of post processing.

The challenges encountered by AM echo those found in the casting industry. Like castings, AM preforms must contain the final part with sufficient material to achieve required form and finish, have adequate stiffness to support finishing operation forces, be able to be accurately located in a machine work volume, and meet strength requirements. They generally do not have well defined surfaces for referencing and can be difficult to precisely orient and locate relative to a machine tool reference frame without time-consuming metrology or special fixturing. Often many iterations of a preform must be produced and measured before each of these requirements are met. The result is wasted material, long lead times, and an overbuild final part. Hybrid manufacturing has been introduced as a method for addressing these challenges.

In hybrid manufacturing, additive and subtractive processes share a common work volume and coordinate system. The term is sometimes extended to include multi-machine and work cell configurations. In this dissertation hybrid manufacturing is more narrowly defined as the combination of two or more processes in the same work volume that improves productivity or creates new design space. A hybrid machine tool and process offer capabilities that separate machines cannot. Integrating directed energy deposition (DED) into existing computer numerical control (CNC) machine tools enables part repair, cladding, selective feature deposition, and full component deposition. New designs are possible from the ability to create internal geometry, such as conformal cooling channels, tunable dynamics, and multiple materials to locally optimize toughness, conduction, or hardness, for example. To maximize the potential of these new systems and processes, traditional process models need to be updated. This work focuses on the development of new metrology and modeling tools for milling in a hybrid process.

With the ability to alternate between deposition and machining, several manufacturing approaches are available, presented in order of increasing complexity. The first and most common approach is to complete all of the deposition first, let the part cool, and then complete the finish machining, effectively serializing the process. Errors from thermal stress, thermal expansion, or errors during material deposition are fully developed prior to the machining stage. This creates clear division between

the additive and subtractive aspects of the process, allowing for the use of traditional techniques and modeling for each. Using previous definition, this approach does not quality as hybrid manufacturing. The second option is an iterative hybrid approach, where some number of layers are deposited, that section is machined, and deposition continues. Using this strategy previously impossible internal features can be machined and the need long flexible tooling can be reduced, increasing productivity. The third strategy is simultaneous deposition and machining, with a theoretical goal of matching the deposition and metal removal rates.

The latter two approaches overlap between the additive and subtractive processes, changing the dynamics of both. With respect to milling, the largest effect can be seen on the workpiece temperature. In conventional milling, the bulk workpiece temperature remains well below the working limit of the material, generally near ambient. Workpiece temperatures in hybrid manufacturing are dynamic. They begin at the melting temperature during deposition and decrease with time as the material solidifies and cools, repeating each layer. Local temperatures can exceed 1500°C and bulk temperatures can exceed 300°C depending on material, part geometry, and deposition strategy [6].

Models for conventional milling process models use material dependent cutting force coefficients, tool dynamics, workpiece dynamics, and chip area to calculate cutting force and stability limits. At elevated temperatures, however, these coefficients, the workpiece dynamics, and the chip area all change. For example, thermally assisted machining, where a high intensity heat source is used to heat the tool-chip interface, can reduce cutting forces by 60% [7]. A model that does not incorporate temperature effects will generally overestimate the cutting force and workpiece dynamics stiffness and underestimate the chip area. Milling parameters that are stable at ambient conditions may be unstable at higher temperatures, leading to unexpected chatter, a self-excited vibration that results in large cutting forces and vibration, and less than optimal milling performance.

Cutting force coefficients are calculated for a particular tool/material combination using measured cutting forces over a range of feed rates. In this work, a metrology

system was designed, constructed, and tested for the measurement of cutting force for a workpiece at elevated temperatures. Bulk temperatures of up to 500°C are possible. Introducing temperature into a metrology system is challenging, because spatial and temporal gradients tend to reduce the measurement performance. Previous research on thermally enhanced machining used an intense small diameter heat source to locally soften the material just ahead of the cutting tool. The bulk material temperature does not increase so traditional measurement methods may be applied. In hybrid manufacturing, on the other hand, the bulk material temperature is elevated and not localized to the tool-chip interface. To better simulate the hybrid manufacturing process and mimic the global heating, a constant temperature approach was selected. Workpieces were heated to and held at a constant temperature while cutting forces were measured, while minimizing thermal gradients by platform design. Forces were measured at discrete temperatures to identify relationships between temperature and cutting force coefficients. Given this information, improved process prediction is made possible.

Hybrid manufacturing is a relatively immature process that has the potential to leverage the best aspects of additive and traditional subtractive manufacturing to enable the production of a new class of parts. Before it can be adopted by the larger manufacturing community, the operating efficiency and manufacturing capabilities must outweigh the high capital investment. Developing better process models will enable improved cycle time, part quality, and accelerate advanced manufacturing techniques.

Chapter 2

Literature Review

This chapter covers the technical background and previous research in three topic areas: machining dynamics, thermally enhanced machining, and hybrid manufacturing. Machining dynamics is the application of mechanical vibrations to machining process modeling. Using cutting force models, which include empirical material specific cutting force coefficients, and tool-holder-spindle-machine frequency response functions (FRFs), milling parameters can be selected to maximize process efficiency. Milling at elevated temperatures in a hybrid, the topic of this research, is form of thermally enhanced machining (TEM), where material is heated to reduce cutting forces. As cutting forces and workpiece dynamics change in hybrid manufacturing, optimal milling parameters also change. While a large body of research exists for milling modeling and prior research has been conducted in TEM, primarily for single point turning, its application to elevated temperature milling during hybrid manufacturing is limited. In TEM turning, for example, the tool orientation does not change, so it is straightforward to integrate a point heat source ahead of the cutting edge. In milling, however, the cutter rotates and changes feed directions, so a point heat source is difficult to implement. In hybrid manufacturing, on the other hand, the heat source is deposition, raising the bulk temperature of the workpiece as the part is built, and the temperature profile ahead of the cutting tooth does not change with

cutting tooth direction and orientation. Incorporating the influence of temperature on the milling process, including the cutting force, chip area, and structural dynamics, advances current modeling capabilities and enables hybrid manufacturing efficiency to be increased.

2.1 Machining dynamics

The basics for today's machining dynamics models were established in the late 1950s. The study of machining dynamics provided the groundwork for the next wave of manufacturing productivity [8, 9, 10, 11]. The associated machining models can be used to improve milling productivity, which is measured using metrics including spindle up time, overall cycle time, cost, and metal removal rate (MRR) [12]. From a machining dynamics perspective, the goal is to maximize the MRR without introducing significant part errors or increasing tooling costs [13]. Limits to productivity include system stiffness, spindle and axis motor power, controls, workpiece cooling, and chip evacuation, to name a few. These limits are fixed characteristics of a particular machine. In order to improve MRR, therefore, process parameters must be selected that respect and maximize machine limitations.

Cutting tools, spindles, machines, and workpieces are not rigid. Each component can be modeled as a mass-spring-damper system. Because each component has some flexibility, forces generated from the cutting process cause deflection and vibration at the tool tip (where material removal occurs). The vibration amplitude is determined from the magnitude and frequency of the cutting force and the system dynamics. The tool tip vibration causes a variation in chip thickness, h, and a corresponding change in cutting force, as shown in Equations 2.3 to 2.3. The chip thickness is therefore a function of time, where the current value depends on both the commanded chip thickness, the current vibration, and the surface left by the previous tooth. If the chip thickness and force increase with each rotation until a process limit is reached, the cut is unstable [10]. The forces increase until the tool breaks or leaves the workpiece. Regenerative chatter is characterized by unstable vibrations at the tool tip that causes

poor surface finish, part errors, rapid tool wear, and tool breakage. A simulation result for unstable milling is shown in Figure 2.1. Figure 2.2 shows a simplified model of regenerative chatter in turning, note the phase difference between the two surfaces.

$$h = f_r \tag{2.1}$$

$$h(t) = h_m + y(t-\tau) - y(t) \tag{2.2}$$

$$F = K_s b h(t) \tag{2.3}$$

Where h = commanded chip thickness; f_r = feed per rev; $h(t)$ = time dependent chip thickness; F = resultant cutting force, K_s = specific cutting force.

The cutting force is depends on the phase between the current and previous tool vibration. Stability in turning depends on the chip width, b, and spindle speed, Ω. The limiting chip width, defined as the maximum chip width stable at a selected spindle speed, is dependent on the material specific cutting force, K_S, and the system dynamics, represented by the frequency response function (FRF). K_s is an empirical coefficient that relates force and uncut chip area for a particular material-tool geometry combination as shown in Equation 2.3. Analytical relationships for a frequency domain turning stability model are given in Equations 2.4-2.6 [12].

$$b_{lim} = \frac{-1}{2K_s cos(\beta) Re[FRF]} \tag{2.4}$$

$$\frac{f_c}{\Omega} = N + \frac{\epsilon}{2\pi} \tag{2.5}$$

$$\epsilon = 2\pi - 2\tan^{-1}\frac{Re[FRF]}{Im[FRF]} \tag{2.6}$$

Where b_{lim} = limiting chip width, β = angle between the resultant (F) and normal force (F_n), f_c = chatter frequency, ϵ = phase between the current and previous tool vibrations, N = the integer number of waves of vibration imprinted on the workpiece per revolution.

As noted, the system dynamics are characterized by the FRF. The complex valued

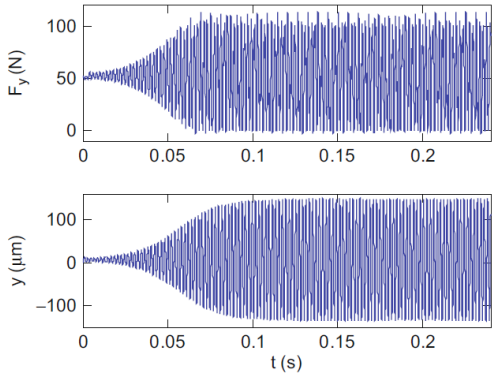


Figure 2.1: Unstable simulation results for force (top) and displacement (bottom)

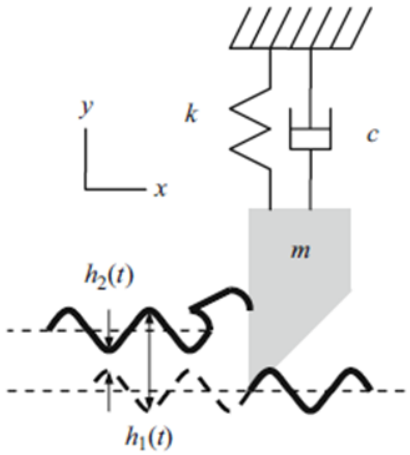


Figure 2.2: Chip thickness variation simplified [13]

FRF is defined as the ratio of the displacement to the input cutting force over a range of frequencies, f. The FRF may be plotted as the real part versus frequency and imaginary part versus frequency. The imaginary peak for each vibration mode is located at the system's natural frequency. Examples of a single degree and multi degree of freedom system are shown in Figures 2.3 and 2.4, where the natural frequency is 500 Hz. The FRF for systems with known mass, stiffness, and damping values can be plotted analytically. In practice, the FRF is measured and then a model is defined by modal fitting. Measurement and fitting can be performed for both the tool and workpiece and superimposed to model the dynamic system.

There are many methods used to measure FRFs. The basic hardware includes: a mechanism for known force input across a range of frequencies, a transducer to measure the response, and a dynamic signal analyzer to record both signals [13]. One of the most common methods is impact testing. In this case, an instrumented hammer is used to generate an impulse that excites a broad range of frequencies. The response is measured as displacement (capacitance gauge), velocity (laser Doppler vibrometer), or acceleration (low mass accelerometer). For milling stability modeling, the frequency dependent ratio of the displacement to the input force, or receptance, is required.

The analytical model presented in Equations 2.4-2.6 provides a global view of stability turning stability. Modifying for the milling process requires a fixed average tooth angle and average force direction to be assumed.

$$b_{lim} = \frac{-1}{2K_s Re[FRF_{orient}]N_t^*} \tag{2.7}$$

$$\frac{f_c}{\Omega N_t} = N + \frac{\epsilon}{2\pi} \tag{2.8}$$

$$\epsilon = 2\pi - 2\tan^{-1}\frac{Re[FRF_{orient}]}{Im[FRF_{orient}]} \tag{2.9}$$

$$N_t^* = \frac{\phi_e - \phi_s}{\frac{360}{N_t}} \tag{2.10}$$

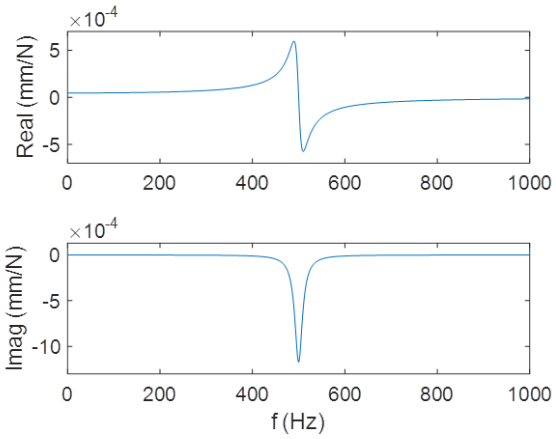


Figure 2.3: Example single degree of freedom FRF.

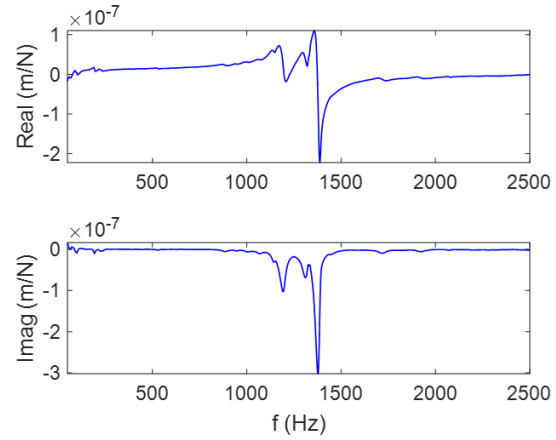


Figure 2.4: Example multiple degree of freedom FRF.

$$FRF_{orient} = \mu_x FRF_x + \mu_y FRF_y \tag{2.11}$$

$$\phi_s = \pi - \cos^{-1}(\frac{r-a}{r}) \quad \phi_s = \pi \tag{2.12}$$

Where $Re[FRF_{orient}]$ = real part of the oriented frequency response, $Im[FRF_{orient}]$ = imaginary part of the oriented frequency response, N_t^* = average number of teeth engaged in the cut; f_c = chatter frequency, Hz; N_t = number of cutting teeth; N = lobe number; Ω = spindle speed, rpm; $\mu_{x,y}$ = directional orientation factor. The start and exit angles, (ϕ_s and (ϕ_e are given in radians for a down/climb milling direction.

The frequency domain analytical solutions for milling and turning do not predict cutting force or tool vibrations [13]. To compliment the analytical stability map, a numerical time domain simulation can be used to calculate the time dependent cutting force and vibration for a given system and set of milling parameters. Subsequently, the milling stability can be determined using the force or vibration signals. The simulation applies numerical integration to solve a set of second order time delayed differential equations of motion [14]. First the instantaneous chip thickness, $h(t)$, is calculated using the vibration of the current and previous cutting tooth; see Equation 2.14 and Figure 2.5. The cutting force is calculated using the instantaneous chip area and cutting force coefficients and shown in Equations 2.15 and 2.16. This force is used to find the new displacement by Euler integration, the tooth angle is incremented (i.e. the cutter is rotated to the next orientation), and the process is repeated. An example of the force output is provided in Figure 2.6. Periodic sampling of the output signals can be applied to automatically differentiate between stable and unstable behavior. If the sampled points repeat, the behavior is stable (forced vibration). If they do not, it is unstable (self-excited vibration) [15, 16, 17].

Step 1: The instantaneous chip thickness is calculated.

$$n = xsin(\phi) - ycos(\phi) \tag{2.13}$$

$$h(t) = f_t sin(\phi) + n(t-\tau) - n(t) \tag{2.14}$$

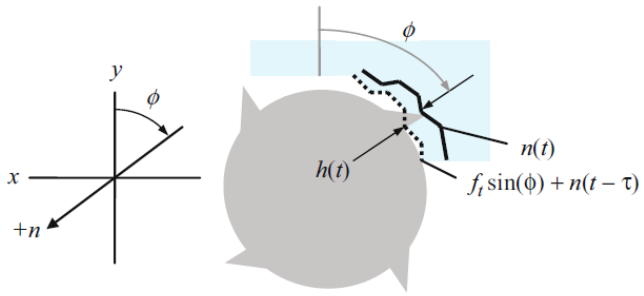


Figure 2.5: Geometry of instantaneous chip thickness calculation for milling [13]

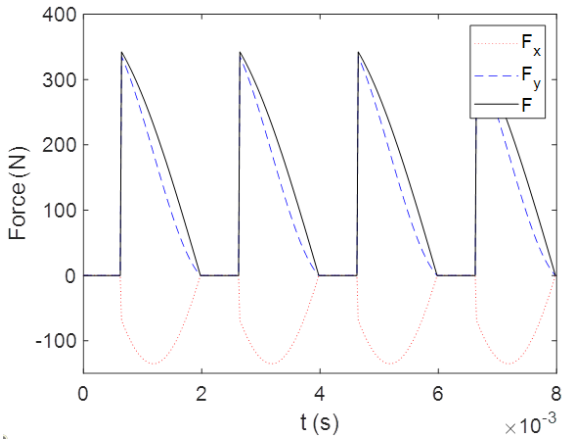


Figure 2.6: Example time domain 25% radial immersion down milling cutting force components [13]

Where $h(t)$ = instantaneous chip thickness, ϕ = cutter angle, τ = tooth period, n = surface normal

Step 2: The cutting force is calculated and transformed into the x, (F_x) and y, (F_y), directions.

$$F_n = k_n bh + k_{ne} b \qquad\qquad F_t = k_t bh + k_{te} b \tag{2.15}$$

Where F_n = surface normal force projection, F_t = tangential force projection, k_t = tangential cutting force coefficient, k_n = normal cutting force coefficient, $k_t e$ = tangential edge cutting force coefficient, $k_n e$ = normal edge cutting force coefficient, b = axial depth of cut (ADOC), h = chip thickness.

$$F_x = F_n sin(\phi) + F_t cos(\phi) \qquad\qquad F_y = -F_n cos(\phi) + F_t sin(\phi) \tag{2.16}$$

Step 3: New velocities and positions are determined by Euler integration. The system equations of motions are defined using the modal stiffness, k_q, modal damping ratio, c_q, and modal mass m_q, with subscripts x and y denoting direction.

$$\ddot{x} = \frac{F_x - c_{qx}\dot{x} + k_{qx}x}{m_{qx}} \qquad\qquad \ddot{y} = \frac{F_y - c_{qy}\dot{y} + k_{qy}y}{m_{qy}} \tag{2.17}$$

$$\begin{aligned} \dot{x} &= \dot{x} + \ddot{x}dt \quad \dot{y} = \dot{y} + \ddot{y}dt \\ x &= x + \dot{x}dt \quad y = y + \dot{y}dt \end{aligned} \tag{2.18}$$

From the process described in Equations 2.13 to 2.18, the inputs required for the time domain simulation are: modal parameters m_q, k_q, c_q to describe the tool tip dynamics, cutting force coefficients $k_n, k_n e, k_t, k_t e$, and cutting parameters $\Omega, \phi_s, \phi_e, b, h, N_t, d$ and γ, where d is the tool diameter and γ is the tool helix angle.

The mechanistic cutting force coefficients k_n, k_t, k_{ne}, and k_{te} correspond to the normal, tangential, and edge components (e subscripts) of the cutting force respectively.

The normal and tangential coefficients are associated with cutting (or shearing) and the edge coefficients are independent of chip thickness and associated with rubbing (i.e., edge effects). The normal cutting force (F_n) and tangential cutting force (F_t) are calculated using the corresponding coefficients, the chip width (b), and chip thickness (h), as in Equation 2.15.

It is important to note that the cutting force coefficients depend not only on the workpiece material properties, but also on the tool geometry (e.g., rake and relief angles for the cutting edge). They can be determined experimentally using a linear regression analysis of the average cutting force in the x and y directions measured over a range of feed per tooth values. Both the mean x and y forces are required as the modal parameters are defined in the x-y coordinate system. The mean cutting forces in x, $\overline{F}_x$, and y, $\overline{F}_y$, are defined in Equation 2.19.

$$\begin{aligned} \overline{F}_x &= \left[\frac{N_t b f_t}{8\pi} (-k_t \cos 2\phi + k_n (2\phi - \sin 2\phi + \frac{N_t b}{2\pi} (k_{te} \sin \phi + k_{ne} \cos \phi) \right]_{\phi_s}^{\phi_e} \\ \overline{F}_y &= \left[\frac{N_t b f_t}{8\pi} (k_n \cos 2\phi + k_t (2\phi - \sin 2\phi + \frac{N_t}{2\pi} (k_{te} \cos \phi + k_{ne} \sin \phi) \right]_{\phi_s}^{\phi_e} \end{aligned} \tag{2.19}$$

Where N_t = number of cutting teeth; f_t = feed per tooth; ϕ_e = cut exit angle; ϕ_s = cut start angle, see Figure 2.7.

The analytical and time domain solutions can be used to generate a stability map, plotting the limiting axial depth of cut, b_{lim}, for a particular spindle speed, see Figure 2.8. When b_{lim} is calculated for a range of spindle speeds, the result is a stability map. The analytical stability map is generated by: 1) determining the oriented FRF and identifying the valid chatter frequency range(s), f_c; 2) solving for ϵ (Eq. 2.9), the phase between the current and previous tooth vibrations over the valid frequency range(s); 3) finding the average number of teeth engaged, N_t^*, (Eq. 2.10); 4) calculating b_{lim}, (Eq. 2.7); 6) and plotting Ω vs. b_{lim} [13]. The time domain stability map is generated by determining stability at a range of discrete points, Figure 2.10.

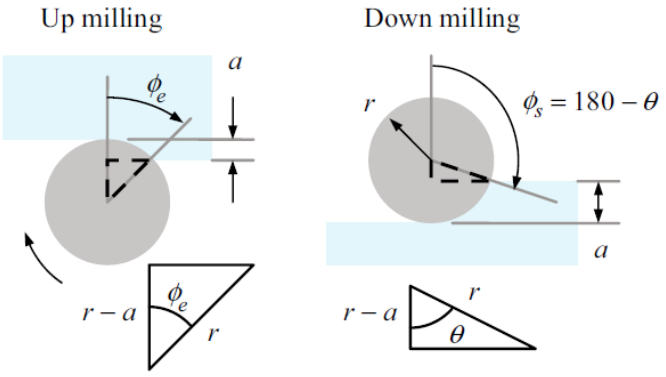


Figure 2.7: Exit and start angle geometry for up and down milling. [13]

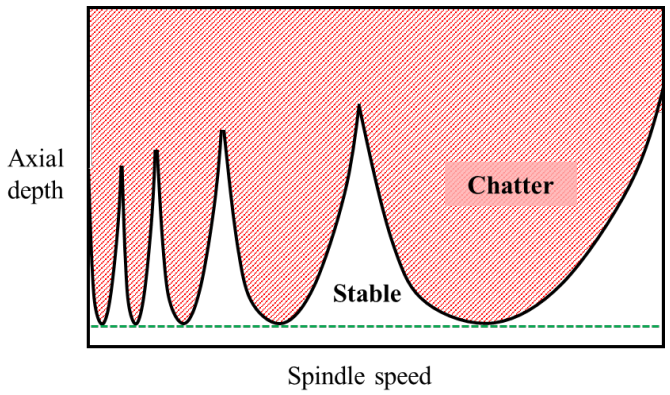


Figure 2.8: Example analytic stability map

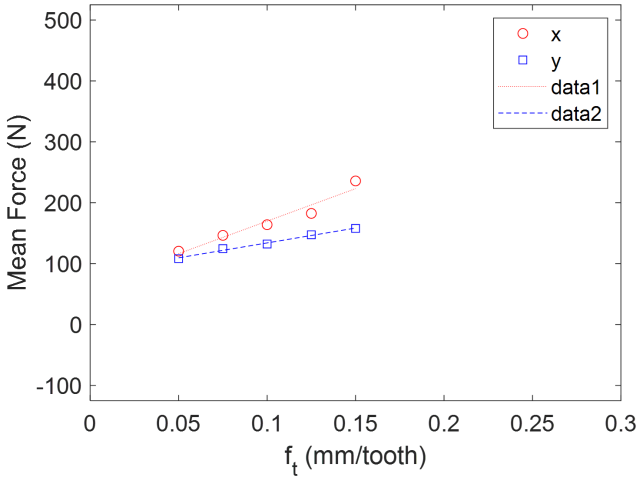


Figure 2.9: Cutting tests for coefficient linear regression.

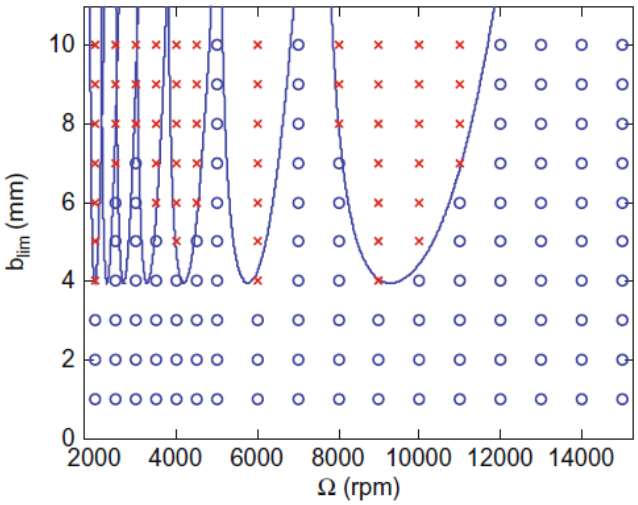


Figure 2.10: Example simulated stability map

Regions below the limit are stable and regions above the limit are unstable. Selecting a stable operating point with the highest available axial depth at the corresponding spindle speed maximizes the metal removal rate and increases productivity. Stability maps can also be generated using time domain simulation. Simulations are completed over a grid of axial depth of cut and spindle speeds, stability is determined for each grid point, and the results are plotted to identify the stability boundary. This method is computationally intensive as many simulations must be performed to create a high-resolution stability boundary, but assumptions in the analytical solution are removed.

The stability boundary can be increased by either changing the tool and workpiece system dynamics (stiffness and damping) or changing the cutting force coefficients. Generally, the workpiece material and geometry are fixed, and the cutting tool has been chosen to maximize stiffness. Without changing the tooling, reducing the cutting force coefficients is the primary way to globally increase the limiting axial depth of cut and maximize the metal removal rate. One way to achieve this coefficient reduction is with thermally enhanced machining.

2.2 Thermally enhanced machining

Thermally enhanced machining was developed to increase the machinability of high strength and heat resistant materials. An external source heats the area directly in front of the cutting tool to soften the material, Figure 2.11. As a result, the yield strength, hardness, and strain hardening behavior all decrease, reducing cutting force and, in some cases, reducing tool wear. This increases the maximum allowable MRR, decreases manufacturing costs, and increases productivity [18].

Heat sources include gas flame [19], induction [20, 21, 22], plasma [23, 24, 7], and laser beam [25, 26, 27]. Additive deposition has yet to be studied as a heat source. As laser costs have fallen, laser assisted machining (LAM) has become a more common approach for heating the workpiece during turning and milling applications. In most experimental setups the workpiece is heated directly in front of the cutting tool to

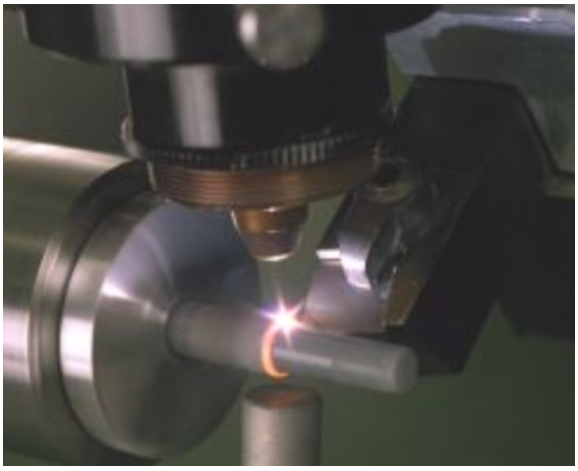


Figure 2.11: Laser assisted turning [30]

localize the heat input and minimize the heat transferred to the workpiece, reducing or eliminating any heat affected zones, and increasing the process efficiency. To penetrate to the full axial depth of cut, the temperature ahead of the cutting zone must overshoot the desired temperature. This results in the material in front of the cutting edge having a non-uniform temperature distribution that is dependent on the heat input and chip area, see Figure 2.12. It is difficult to predict, measure, and control the temperature at the cutting edge.

The first applications of thermally assisted machining were turning operation due to the ease of setup. In single point turning, the tool and heating element are stationary, and there is a uniform chip thickness, allowing for even heating throughout the uncut chip area . The first thermally assisted machining patent was granted in 1889 to Tilghman [28]. An electric current was used to heat successive portions of the surface to soften it before abrading or cutting. In 2006 a patent was granted for a "Laser assisted machining method device", using a laser to soften the workpiece in a turning operation. Milling applications are more challenging because the cutting tool direction changes, the width of cut can require a large heating area, the cut is interrupted, and the chip thickness is variable, Figure 2.13. To accommodate large radial depths of cut, several strategies are used: focus the heat source at the entrance of the cut or at the average width; raster the seat source over the entire radial area; or integrate the laser into the cutting tool, shown in Figure 2.14. [29].

Cutting force in thermally assisted machining has been measured for a variety of materials, processes, and temperatures. Commonly studied materials are heat resistant super alloyss (HRSAs) (such as Inconel, Monel, and Waspaloy), titanium alloys, hardened steels, and stainless steels. Table 2.1 summarizes the results of prior experiments. In all cases and materials, the cutting force decreased as the material temperature increased. The increase in temperature at the primary shear zone reduces the yield strength and work hardening of the workpiece, decreasing the force required to shear the chip [18]. The average shear plane length and thickness also tend to decrease with temperature [32]. Rao [33] and Davami [34] show that heating the workpiece can improve surface quality. This effect is attributed to the

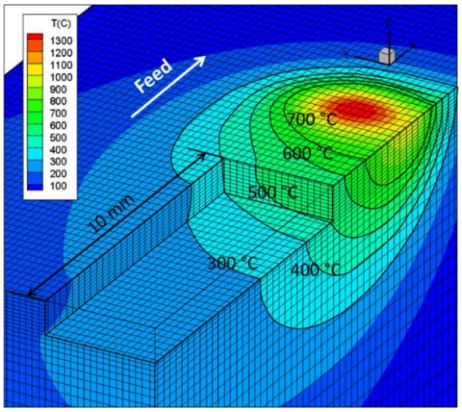


Figure 2.12: Simulated temperature distribution for laser assisted machining of Ti-6Al-4V [31]

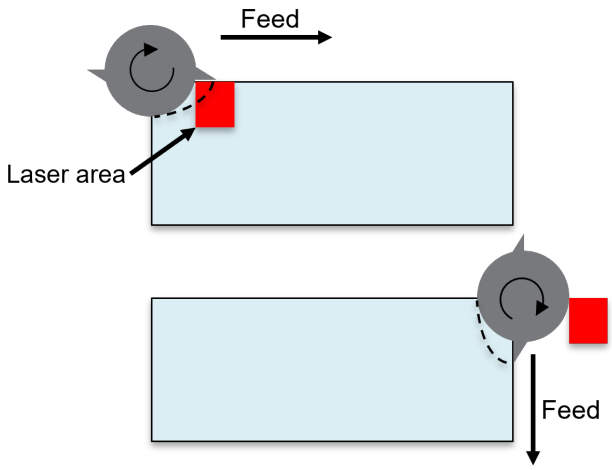


Figure 2.13: Challenges in integrating LAM into a milling process. The red square shows that a fixed location heat source is not adequate for milling operations in different directions.

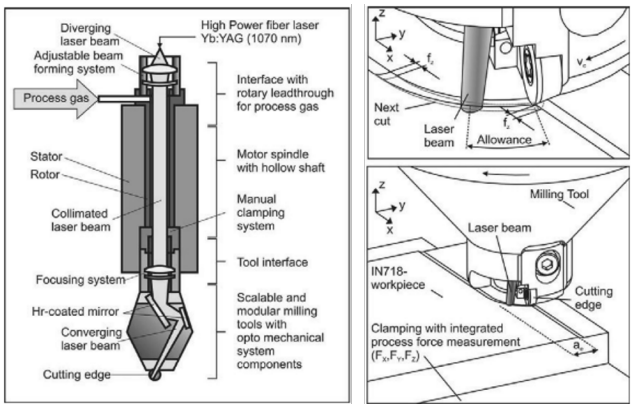


Figure 2.14: Laser assisted milling with integrated optics [29].

reduction in cutting force and changes in the shear plane, causing a change in the chip morphology from discontinuous to continuous.

Modeling cutting force in thermally assisted machining has received less attention in the literature than measured force reduction. Pan [25] focused on recrystallization effects for the force modeling of laser assisted milling of Inconel 718. The recrystallization effects were incorporated by applying a grain size-dependent parameter in the Johnson-Cook model. The maximum error between predicted and measured cutting force was reduced to less than 20%. The softening effect was attributed to elongated grain size and grain growth in the shear zone instead of flow softening. Zamani [35] and Xi [36] used 3D finite element model simulation and the Johnson-Cook material model, modified for very high strain rates and system temperatures, to predict cutting force in Ti-6Al-4V. They reported good agreement between simulated force in the y and Z directions, with higher force than predicted in x (feed direction). No work has been found using a mechanistic force model and time domain simulation to predict cutting force and tool displacement in thermally assisted machining.

There is evidence that for certain cutting parameters, elevated workpiece temperatures increase tool life or increase the MRR for a given tool life, see Figure 2.15 and Figure 2.16. Ozler [21] found as the machining temperature increases, a corresponding reduction in tool wear was observed as a result of the reduction in resistance to machining. It was also reported that a higher cutting speed is usually preferred in hot machining. Tosun [19] studied tool life in hot machining using artificial neural networks and regression analysis. The experiments showed that tool life increased in hot machining of manganese steel and the highest tool life was obtained at 400°C. The results also showed little increase in tool life between 400°C and 600°C, matching Ozler's observations.

Hedberg [31] showed a cutting speed increase of 35% in Ti-6Al-4V while maintaining equivalent tool life with laser assisted machining. The improvement in cutting speed and tool life was attributed to the reduction in built up edge and premature chipping that occurs at high cutting speeds in traditional machining. Figure 2.15 and Figure 2.16 show the results from Hedberg and Parida, plotting tool wear (as flank wear

Table 2.1: Summary of cutting force results for thermally enhanced machining

Source	Material	Process	Heat source	Pre-heat temp (° C)	Force reduction (%)
Moon [7]	AISI 1045	Milling	Plasma	700	60
Lopez [23]	Haynes 25	Milling	Plasma	700	29
Leshock [37]	Inconel 718	Turning	Plasma	350	30
Lopez [23]	Inconel 718	Milling	Plasma	800	45
Brecher [29]	Inconel 718	Milling	Laser	600	40
Moon [7]	Inconel 718	Milling	Plasma	900	57
Parida [38]	Monel 400	Turning	Gas torch	600	60
Baili [22]	Ti-5553	Turning	Induction	650	28
Ginta [39]	Ti-6Al-4V	Milling	Induction	650	22
Hedberg [31]	Ti-6Al-4V	Milling	Laser	500	22
Zaeh [40]	Ti-6Al-4V	Milling	Laser	800	13
Rashid [41]	Ti-6Cr-5Mo	Turning	Laser	1100	15

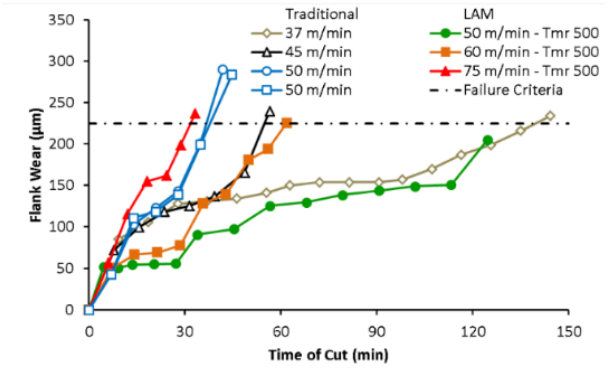


Figure 3.7: Ti-64 tool wear for traditional milling and LAML using a KC520 insert.

Figure 2.15: Ti-6Al-4V tool wear for traditional milling and laser assisted milling [31]

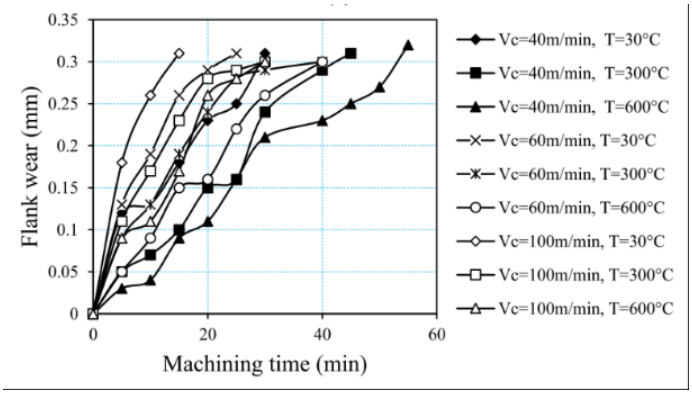


Figure 2.16: Tool wear in Monel 400, Vc is surface speed in m/min [32]

width) for a range of surface speeds and temperatures. Thermal softening of the tool material also occurs at elevated temperatures; see Table 2.2.

There is limited prior work on predicting or measuring the stability of thermally assisted machining. Ginta [39] and Amin [42] observed the reduction of vibration amplitude at select frequencies. Up to 12,500 Hz, the maximum acceleration amplitude was reduced an average of 50% when the workpiece was heated to 650°C [21]. Stability was not directly addressed. Uhlmann [43] heated 7075 aluminum to 100°C and measured the cutting forces with a dynamometer. The results showed decreasing specific cutting force with increasing workpiece temperature and positive changes in the stability boundary, see Figure 2.17. Future work of implementing a stability prediction tool for elevated temperatures was recommended.

2.3 Hybrid manufacturing

Metal additive processes can be separated into two categories based on material delivery: wire-fed and power-based systems. These systems use a heat source to locally melt and fuse metal wire or powder and deposit material. Parts are deposited layer by layer until complete. Common heat sources are electric arc, laser beam, and electron beam. Wire fed systems are generally inexpensive to setup and have the highest metal deposition rate. The resolution is limited due to the coarseness of the weld beads, with the minimum bead width usually a multiple of the wire diameter. The surface finish is dominated by the ridges formed between the bead layers. Wire deposited parts almost always must be finish machined to be used as a functional part.

Powder based systems are significantly more expensive but have higher resolution, down to the spot size of the laser/electron beam or, theoretically, the minimum powder size. The high cost comes from the laser and electron beam systems, optics, and the vacuum required for electron beams. There are two types of powder-based additive systems, powder bed and blown powder. Powder bed systems spread a thin layer of metal powder, use a laser or electron beam to melt the desired areas

Table 2.2: Summary of cutting tool material properties

Tool material	Elastic modulus (GPa)	Tensile strength (MPa)	Compressive strength (MPa)	Working temp (°C)
High-speed steel	200	1200	3250	650
Tungsten carbide	670	344	6200	1000
Ceramic (Al2O3)	400	69	3000	1350

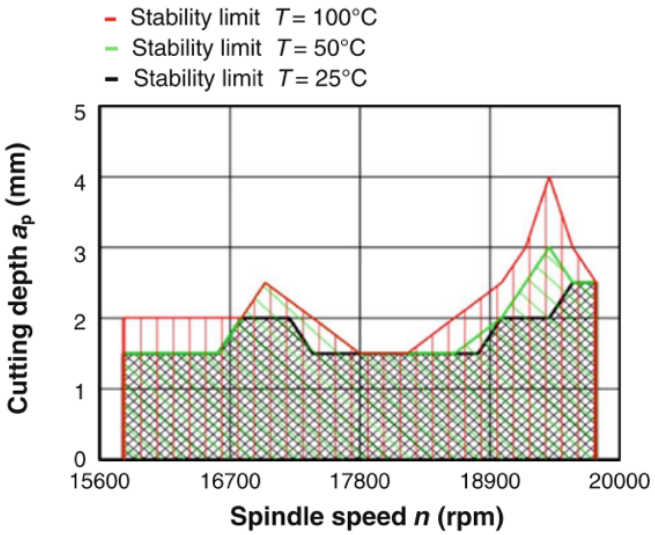


Figure 2.17: Stability limit dependency on temperature, for 7075 aluminum [43]

in that layer, lower the part on an elevator, spread another thin layer on top of the exposed layer, and repeat. Blown powder systems spray metal powder into a melt pool, usually formed by intense, local heating from a laser or electron beam.

Independent of the process, a significant amount of energy from deposition is transferred from the melt pool to the workpiece. With each layer deposited, the part temperature continues increase up until a steady state temperature distribution is reached. The temperature depends on the process, material, part geometry, and deposition parameters. Inter-pass temperatures can reach between 200°C and 1200°C depending on the distance from the last deposited layer [6, 44, 45]; see Figure 2.18. This temperature range overlaps with the temperatures of interest in thermally assisted machining techniques.

As shown in Section 2.2, as the workpiece temperature changes, the cutting force, tool life, and stability map also change. After a particular tool-material dependent temperature, tool wear and failure increases rapidly from a significant rise in built up edge [16] and melting in the cutting zone. Therefore, there exists an optimal temperature band for taking advantage of the benefits of thermally assisted machining. As the workpiece cools after deposition, the temperature will pass through this optimal machining temperature band. Hybrid manufacturing systems that have both deposition and machining capabilities can use the heat of deposition as the energy source for thermally assisted machining. To define the optimal machining temperatures, a temperature dependent cutting force and stability model needs to be developed. With a temperature band identified, deposition parameters can be chosen to maximize the time in the ideal temperature zone during machining.

The conventional approach for hybrid manufacturing is to begin machining after deposition has been fully completed and the part has cooled to room temperature. This results in significant machine idle time where neither the deposition head nor spindle is operating. Machining at elevated temperatures can reduce the machine idle time and increase MRR, improving the overall productivity of the hybrid machine.

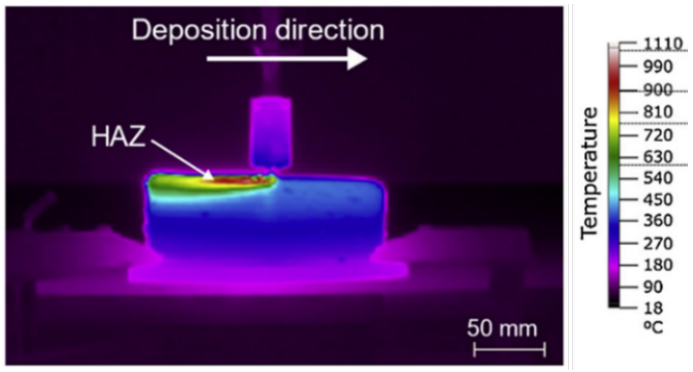


Figure 2.18: Thermographic analysis of WAAM steel [6]

The benefits of thermally assisted machining in hybrid manufacturing are best realized with an iterative build approach. Iterative hybrid manufacturing is the process of producing parts with alternating periods of deposition and machining; see Figure 2.19. Because deposition and machining alternate, the machining of internal features, overhangs, and otherwise impossible geometry is enabled. With this strategy, the temperature of each section can be controlled, and workpiece temperatures during machining can be maintained within the ideal temperature band for maximum MRR.

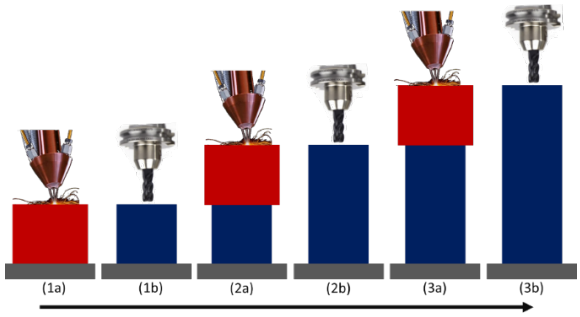


Figure 2.19: Process diagram of iterative additive manufacturing.

Chapter 3

Materials and Methods

As discussed in Chapter 2, the cutting force model used in the time domain milling simulation is based on empirical cutting force coefficients. These coefficients relate the uncut chip area to the cutting force components and are material specific. Easily machinable materials such as aluminum have a specific cutting force, K_s, of around 750 N/mm^2, while more difficult to machine materials such as titanium have a K_s closer to 2000N/mm^2 [12]. The coefficients defined in equation 2.15 are determined by measuring the mean x and y forces and performing a liner regression over a range of feed rates with constant ADOC, radial depth of cut (RDOC), and spindle speed. Measuring the effect of temperature requires adding a heat source and temperature measurement to the dynamometer.

A cutting force dynamometer for measuring cutting force at constant elevated temperatures was designed, constructed, and tested, see Section 3.2 for a visual overview of the system. A constrained motion dynamometer was used to measure the cutting forces and workpiece temperature was measured with a combination of thermocouples and infrared thermography. A high stiffness thermal protection system was developed to isolate the dynamometer from the heat input leveraging a novel insulator developed for the system. To limit the number of variables, a procedure was developed to maintain constant chip width and minimize the effects of temperature

on the force measurement.

3.1 Dynamometer design

Introducing temperature into a cutting force dynamometer produces design and measurement challenges. All materials have an associated coefficient of thermal expansion, which changes geometry with temperature. General practice for manufacturing equipment and measurement transducers is to reject heat sources to maintain a stable temperature [46]. Previous research on thermally assisted machining, however, has used an intense spot heat source to locally soften the material ahead of the cutting zone. Therefore, the bulk material temperature does not increase significantly. This approach approximates the conditions found in processes like laser assisted machining. Hybrid manufacturing, on the other hand, the process is not accurately represented by local heating. In this case the bulk material temperature is elevated by deposition and continuously changes.

Using a local fixed heat source does not allow for a change in cut direction, limiting cutting tests to a single axis. As the material and depth of cut changes, the heat source must be re-calibrated to achieve the target temperature throughout the chip thickness. Local heat sources like laser, plasma, gas torch, and resistance heating are unable to penetrate the full chip thickness without dramatically overshooting the target temperature due to the short heating time. The highest temperature in a laser spot can exceed the material melting point. The temperature gradients and local temperatures at the cutting zone are generally measured using infrared thermography, as it is impractical to use contact measurement during a cutting process [47]. Typical maximum cutting tool temperature measured by infrared thermography has an uncertainty of 50°C [48] due to the associated uncertainty in emissivity. Heating the workpiece to a uniform temperature eliminates these challenges and best represents hybrid manufacturing.

For the elevated temperature cutting force dynamometer designed here, the heating power is provided by 500W, 9.5mm diameter cartridge heaters embedded in a copper

block, collectively referred to as the heating element. The total wattage was calculated to raise the workpiece temperature 480°C in 5 minutes, with a maximum target temperature of 500°C. A proportional-integral-derivative (PID) controller is used to control the heater output with feedback provided by a three wire platinum resistance temperature detector (RTD). The heating element reaches temperatures of up to 1000°C while holding the workpiece at 500°C.

The most common commercially available multi-component force dynamometer has an operating limit of 70°C [49] and costs approximately $100,000. Active liquid cooling would require an unrealistic power density given the size of the workpieces and dynamometer. A failure in the cooling system would cause catastrophic damage to the equipment and create an electrical hazard. A passive insulating layer using traditional rigid thermal insulation does not have adequate stiffness to support cutting operations. The commercially available equipment can therefore not be used for the desired elevated temperature cutting force measurement. The system developed in this section uses a constrained motion dynamometer and novel thermal protection system to measure cutting force at constant elevated workpiece temperature.

3.1.1 Constrained motion dynamometer

The frequency response function (FRF) presented in Chapter 2 showed the relationship between displacement and force (mm/N) in the frequency domain. If the FRF is known, an input force can be inferred using the measured displacement and the inverted FRF (N/mm). This basic principle is used to measure cutting force with a single degree of freedom flexure, referred to as a constrained motion dynamometer, shown in Figure 3.1. The external flanges at the base of the dynamometer are secured to the machine table and the workpiece is bolted to the moving platform. The moving platform produces small displacements when excited by cutting forces. The displacement is measured with a high resolution transducer. This time dependent displacement of the moving platform caused by the milling force is converted to the frequency domain using the Fourier transform, Equation 3.1. It is then multiplied by the inverse of the single degree of freedom (SDOF) dynamometer FRF to determine

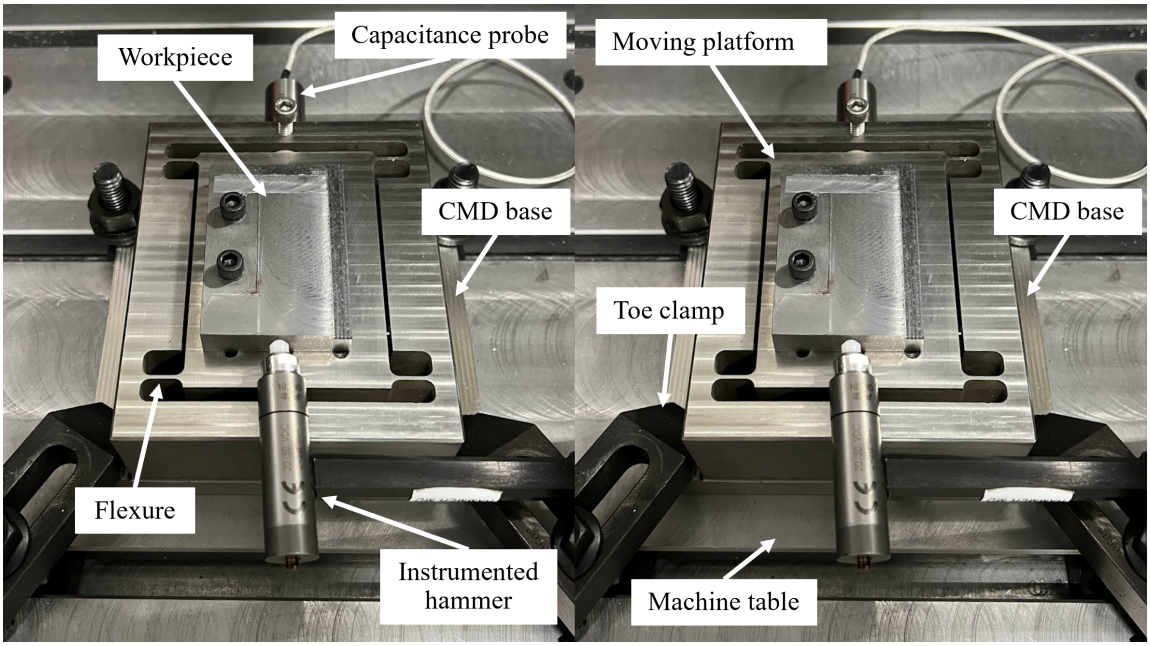


Figure 3.1: Constrained motion dynamometer (CMD) impact testing and components.

the frequency domain force, see Equation 3.2. A low pass digital filter is combined with the inverted FRF to reduce high frequency noise from the displacement signal. Finally the inverse Fourier transform is used to convert back to the time domain to obtain the time dependent cutting force, Equation 3.3 [50]. A detailed analysis of the constrained motion dynamometer (CMD), structural deconvolution, and comparison to a Kistler piezoelectric based dynamometer can be found in [51].

$$X(t) \xrightarrow{\mathscr{F}} X(\omega) \tag{3.1}$$

$$F(\omega) = \left[\frac{X}{F}(\omega)\right]^{-1} X(\omega) \tag{3.2}$$

$$F(\omega) \xrightarrow{\mathscr{F}'} F(t) \tag{3.3}$$

Where: F = cutting force (N), X = measured displacement (mm), $\frac{X}{F}^{-1}$ = receptance ($\frac{\text{N}}{\text{mm}}$), ω = frequency, $\xrightarrow{\mathscr{F}'}$ = inverse Fourier transform, $\xrightarrow{\mathscr{F}}$ = Fourier transform.

The CMD used in this work was a monolithic stainless steel platform constrained by four leaf type flexures. Dimensions of the flexures and other CMD geometry are found in Figure 3.2 and Table 3.1. A capacitance gauge was used to measure the displacement of the moving platform. The system dynamics were measured using impact testing, where a hammer with a force transducer is used to excite the system and the displacement response is measured, as shown in Figure 3.1. The force impulse was imparted at the edge of the workpiece along the center line of the CMD and the response was measured by the capacitance gauge.

While there is no danger of damage to the dynamometer up to roughly 700°C [52], the CMD is sensitive to changes in stiffness caused by temperature changes. The development and testing of the CMD was completed at room temperature conditions, where the system dynamics are constant. To understand the effect of temperature

Table 3.1: Constrained motion dynamometer geometry. Symbols defined in Figure 3.1. E is the height of the CMD, into the page.

Symbol	Value (mm)
t	1.25
r	3.175
L	14.35
A	139.7
B	114.3
C	69.85
D	104.1
E	63.50

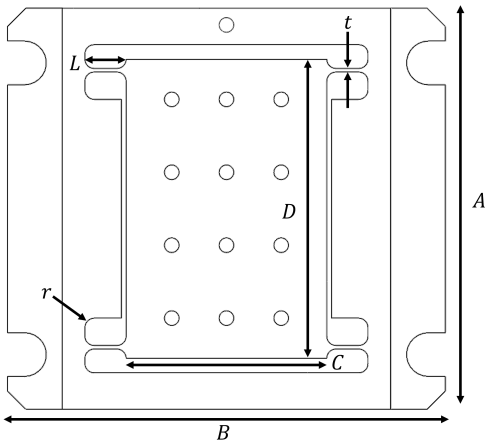


Figure 3.2: Constrained motion dynamometer (CMD) geometry. Dimensions are provided in Table 3.1.

on system dynamics, see the equation for the first natural frequency of a fixed-free beam, shown in Equation 3.4, and the equation for fixed-free beam stiffness shown in Equation 3.5. Both the frequency and stiffness are dependent on the modulus of elasticity and beam geometry. Figure 3.3 shows the change in natural frequency for a 316 stainless steel fixed free beam with temperature, including the effects of a change in modulus and second moment of area. The thermal expansion causes a change in the beam geometry, and therefore the second moment of area. The modulus of austenitic stainless steels decreases linearly from ambient to about 700°C. With the change in modulus, there is a corresponding change in the CMD dynamic stiffness. As temperature increases, the natural frequency and stiffness generally decrease. To capture this variable system response, the system dynamics must be measured over a range of temperatures, adding temperature dependence to the modal parameters extracted from the measured FRFs.

$$f_n = \frac{1}{2\pi}\sqrt{\frac{Ewt^3}{4mL^3}} \tag{3.4}$$

$$k_{beam} = \frac{3EI}{t^3} \tag{3.5}$$

Where f_n= natural frequency (Hz), E= modulus of elasticity (Pa), w= width (m), t= thickness (m),m= mass (kg), L= length (m), k_beam= stiffness of a fixed-free beam

The CMD platform was heated and the FRF measured to evaluate the effect of temperature. Figure 3.4 shows the change in frequency response of the dynamometer over a range of temperatures. The stiffness and natural frequency decreased by 12% from the room temperature value. A changing natural frequency can result in conditions where a set of milling parameters are stable at ambient and unstable at elevated temperatures, Figures 3.5 and 3.6. To maintain sufficient stiffness when machining higher specific cutting force materials such as titanium and stainless steel at high temperatures, the heat flow to the dynamometer should be limited. The capacitance probe has a working limit of 50°C, but is isolated from the bulk of the

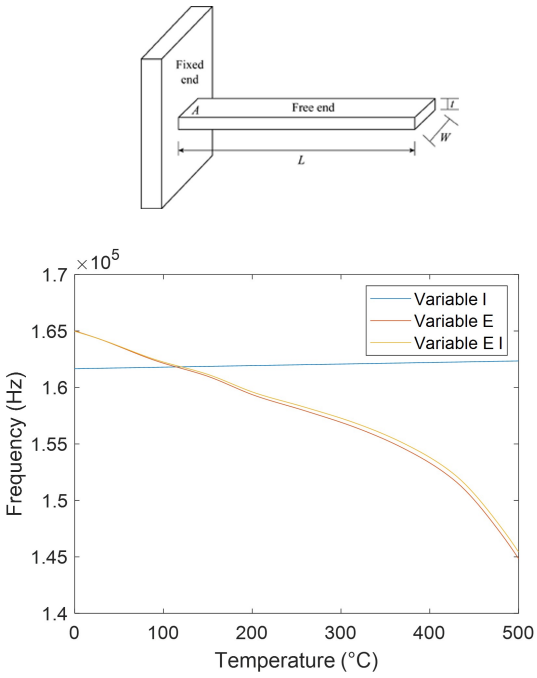


Figure 3.3: Natural frequency vs. temperature for a fixed free beam, see Equation 3.4

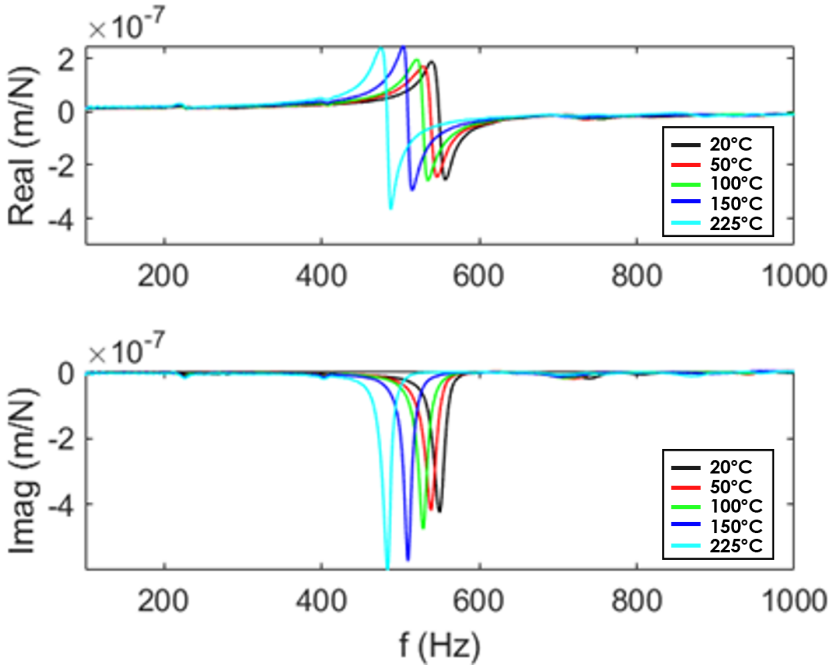


Figure 3.4: Change in FRF with flexure platform temperature.

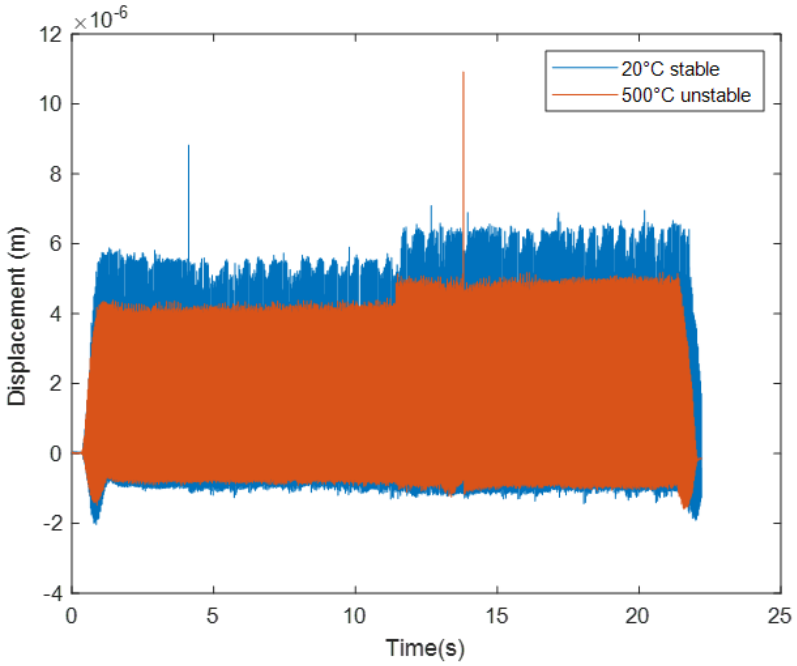


Figure 3.5: Filtered displacement data for a cut that becomes unstable at elevated temperature with constant cutting parameters.

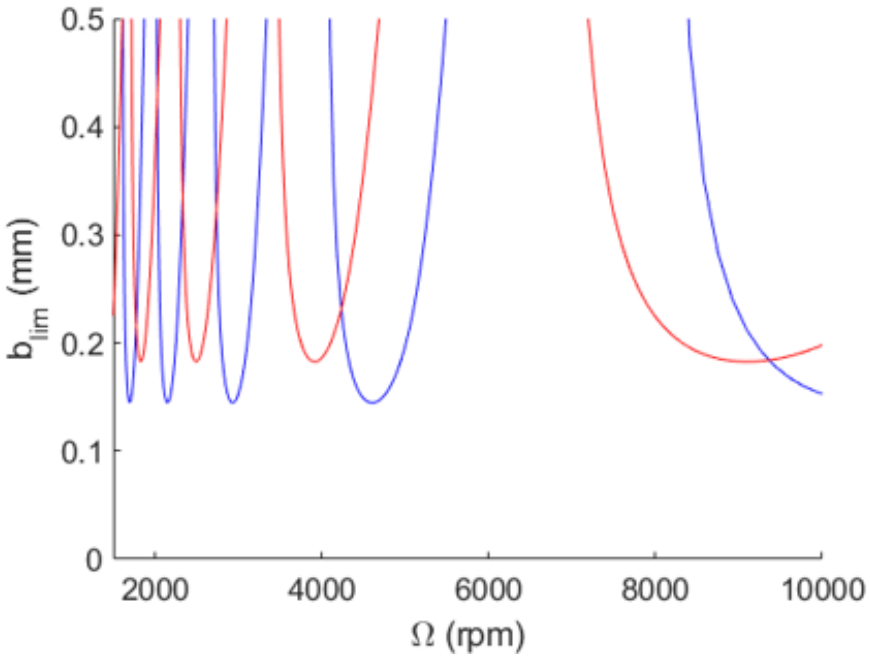


Figure 3.6: Simulated stability lobe diagram. Blue is at 20°C, red is at 300°C.

heat introduced at the platform. The flexure leaves are thin and poor conductors. The dynamometer body is secured to a large steel machine table that acts as a heat sink and keeps the capacitance probe near ambient temperatures.

3.1.2 Thermal protection system

The CMD dynamics the dynamometer itself, the machine table, and anything fixed to the top of the flexure platform. The addition of a workpiece influences the mass, stiffness, and damping of the system. The addition of mass decreases the natural frequency. The modulus and thickness of the workpiece and preload of the fasteners used to secure it to the platform influence the stiffness. At the interface of the part and dynamometer there is interface damping [53]. The more components there are, the larger the cumulative change to the system dynamics. For cutting tests, higher stiffness and natural frequency are desired for stable cutting conditions. A higher CMD natural frequency is desired to avoid resonance (i.e., when the tooth passing frequency matches the CMD natural frequency). The system stiffness must be high enough to support the cutting force and remain stable during cutting, and low enough to generate measurable displacements.

The stackup of components on the flexure platform can be modeled as a series of stiff springs. The compressive stiffness of a material is shown in Equation 3.6. Assuming the area of the workpiece is constrained by the dynamometer area, the modulus and thickness determine the change in stiffness. The stiffness of a stackup of materials, springs in series, is shown in Equation 3.7. The equivalent stiffness is dominated by the lowest modulus element in the series.

When adding a thermal insulator to the system it is critical to maintain the system dynamic stiffness. The minimum selected threshold for the workpiece stackup in this study was that the stackup be ten times stiffer than the dynamometer's most flexible mode. A material with a thermal conductivity of 0.2W/mK and a modulus of 100MPa addresses the flexure heating issue, but significantly reduces the system stiffness. This case is demonstrated in Figure 3.7. Here a calcium silicate insulator

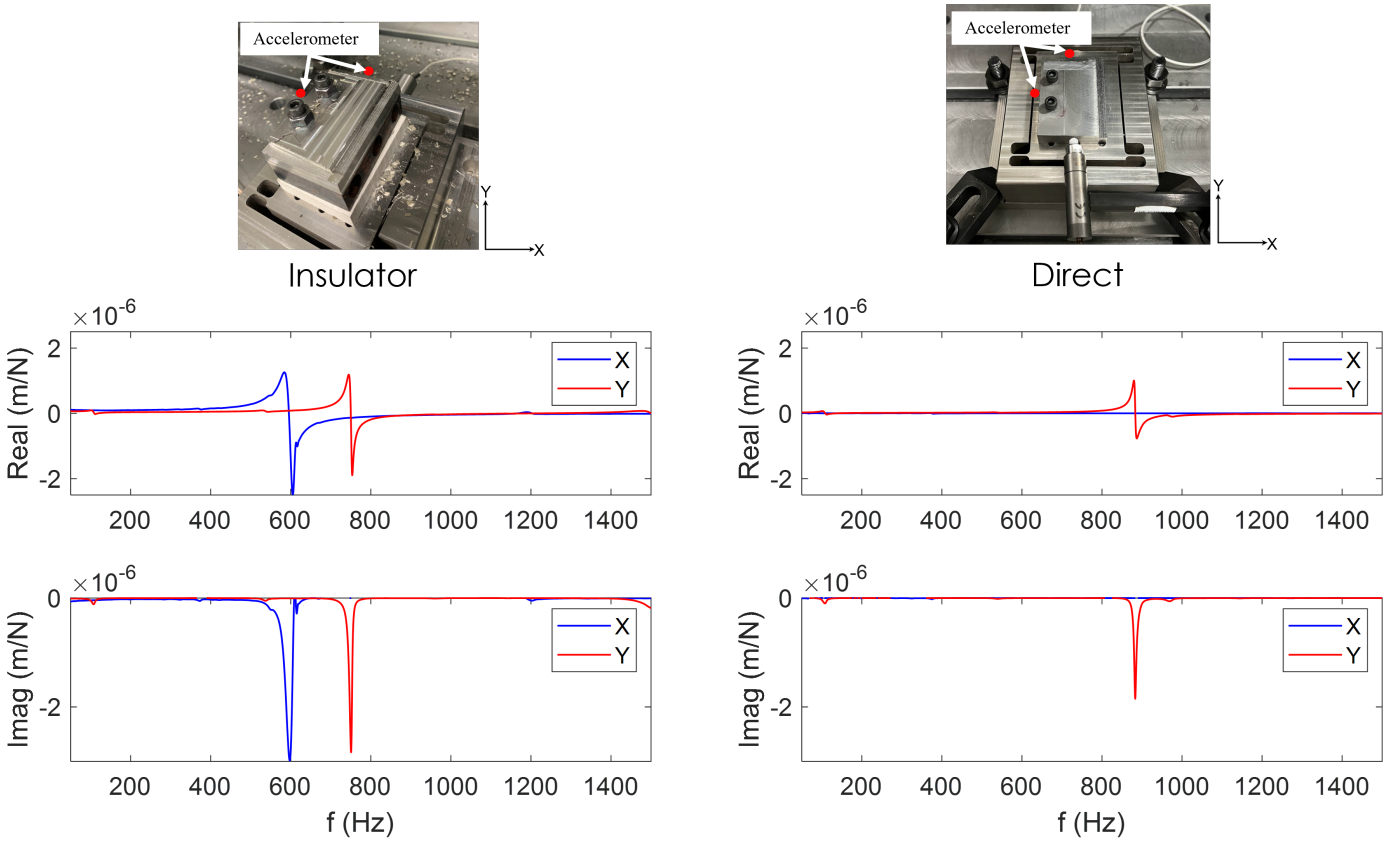


Figure 3.7: Comparison of FRF with (left) and without (right) a rigid calcium silicate insulator. Y is flexible (long) direction, and X the stiff (short) direction.

was placed between the heating element and flexure platform and the frequency response was compared to a workpiece bolted directly to the dynamometer. The low modulus insulator introduced a vibration mode that was more flexible than the dynamometer's most flexible direction.

$$\Delta t = \frac{Ft}{AE} \qquad\qquad k_{compressive} = \frac{AE}{t} \tag{3.6}$$

Where Δt = change in thickness (m), E = modulus of elasticity (Pa), F = force (N), t = thickness (m), A = cross sectional area (m^2), $k_{compressive}$ = compressive stiffness (N/m).

$$k_{beam} = \frac{3EI}{t^3} \qquad\qquad \frac{1}{k_{eq}} = \sum_{n=1}^{\infty} \frac{1}{k_n} \tag{3.7}$$

Where k_{beam} = fixed-free beam stiffness (N/m), I = second moment of area (m^4), k_{eq}= equivalent stiffness (N/m), k_n = component stiffness (N/m).

When evaluating candidate materials, it became evident that there is a correlation between thermal conductivity and elastic modulus, see Table 3.2. The lowest thermal conductivity solid is silica aerogel, with a conductivity of 0.02W/mK, and has a low modulus of 0.042GPa [54]. The lowest conductivity commercially available metal it Ti-6Al-4V, with a higher conductivity of 6.7W/mKand higher modulus of 113GPa. From a materials perspective, as the density of a material increases the thermal conductivity should also increase. Thermal conduction in non-metals is the transfer of a particle's energy to adjacent particles, mainly by collisions. For metals, thermal conductivity is attributed to electron motion. As crystallinity, hardness, and stiffness increase, so does thermal conductivity [55]. Defects like dislocations, grain boundaries, and inclusions negatively impact thermal conductivity. From a geometric perspective, thermal resistance is a function of thickness and area, Equation 3.8. As the material thickness increases or decreases in cross section, the thermal resistance increases.

Table 3.2: Select material properties

Material	Conductivity (W/mK)	Modulus (GPa)	R_t ($\frac{°C}{W}$)	Temp. Limit (°C)
Aerogel	0.02	10×10^{-3}	74	650
Calcium silicate	0.15	7.6×10^{-3}	14	930
G-7	0.29	20.0	12.0	220
Fused silica	1.4	70.0	2.2	1050
Zirconia	2.2	210	1.5	2200
Steatite (L5)	3.0	103	1.1	1200
Ti-6Al-4V	6.7	113	0.5	350
Inconel 718	11.4	205	0.3	705
316 Stainless	16.3	193	0.2	760
1018 Steel	52.0	205	0.06	260

$$R_t = \frac{t}{KA} \qquad\qquad K = \frac{Qt}{A\Delta T} \tag{3.8}$$

Where R_t= thermal resistance (K/W), K= thermal conductivity (W/mK), t= thickness parallel to heat flow (m), A= area perpendicular to heat flow (m^2), Q=heat transfer (W), T=temperature (K)

The thermal protection system design goals were to maximize the stiffness and minimize the heat transfer to the dynamometer. To achieve this with a passive system, a material with a high stiffness and low conductivity was required. The target stiffness is at least 10x higher than the dynamometer's flexible mode at room temperature. Using a simplified model with a stackup of a single insulation layer, copper, and workpiece of an equal thickness of 19mm, the minimum modulus required for the insulator is approximately 2.8GPa. Assuming only conduction through the flexure leaves to an infinite heat sink, the insulator requires a thermal conductivity of 1.5W/mK. The only materials that meet both requirements are G-7 and fused silica. The former has a maximum temperature of 200°C, 800°C below the maximum heater temperature, and the latter has a low bending and tensile strength. Therefore, a new solution was required.

Architected structural insulator

Thermal resistivity as defined in Equation 3.8 has three variables: thickness, thermal conductivity, and cross sectional area. It has been shown that for low modulus materials it is not possible to decrease the thickness enough to maintain both stiffness and thermal properties, and there are no commercially available materials with a high enough modulus and sufficiently low conductivity. Increasing the thickness will increase the thermal resistivity and allow the use of a higher thermal conductivity material, but will decrease the stiffness by increasing the overall height of the stackup, effectively increasing the length of a fixed-free beam. The remaining component is cross sectional area. While the length and width of the insulator are fixed, the cross sectional area at any given plane can be minimized to increase the overall thermal

resistance. In other words, reducing the paths available for thermal conduction can decrease the effective thermal conductivity of a component.

Lattice structures are often used in situations where high stiffness and low mass are required. A similar design strategy can be used to maximize stiffness and thermal resistance. The engineering design and analysis software nTopology was used to model and simulate the stiffness and thermal conductivity of a graph lattice beam. The term graph lattice refers to lattices generated by regularly repeating a unit cell. A selection of unit cells is shown in Figure 3.8 and defined in Table 3.3. Inconel 718 was chosen as the insulator material as it has the highest elastic modulus of any readily printable material and the second lowest conductivity for a metal alloy. More than 800 combinations of unit cells, cell orientations, thicknesses, and cell size were evaluated for the structure shown in Figure 3.9. The thermal conductivity and stiffness were calculated and compared for each iteration. A sample of the simulation results is provided in Table 3.4. The cell types identified in the table were evaluated for a range of thicknesses between 0.75mm and 4mm in 0.25mm increments, cell sizes between $1mm^3$ and $4mm^3$ in 1mm increments including non-symmetric unit cell sizes, and three unit cell orientations.

Compressive stiffness was calculated by applying a 1N force to the top face of the body in the negative Z direction with a fixed boundary condition for the bottom face, see Figure 3.10, and measuring the maximum displacement in the Z direction. Stiffness, k, was calculated by dividing the input force by the output displacement. Equivalent thermal conductivity was calculated by defining a constant temperature restraint of 500°C to the top face and a heat flux of -2.62mW/mm^2 was at the bottom face, see Figure 3.11. The change in temperature across the body was calculated by subtracting the maximum and minimum temperatures. Thermal conductivity was calculated by dividing the product of the thickness and heat power by the product of the change in temperature and cross sectional area, see Equation 3.8. Completing the simulation with a solid body instead of a lattice returned the material's defined thermal conductivity.

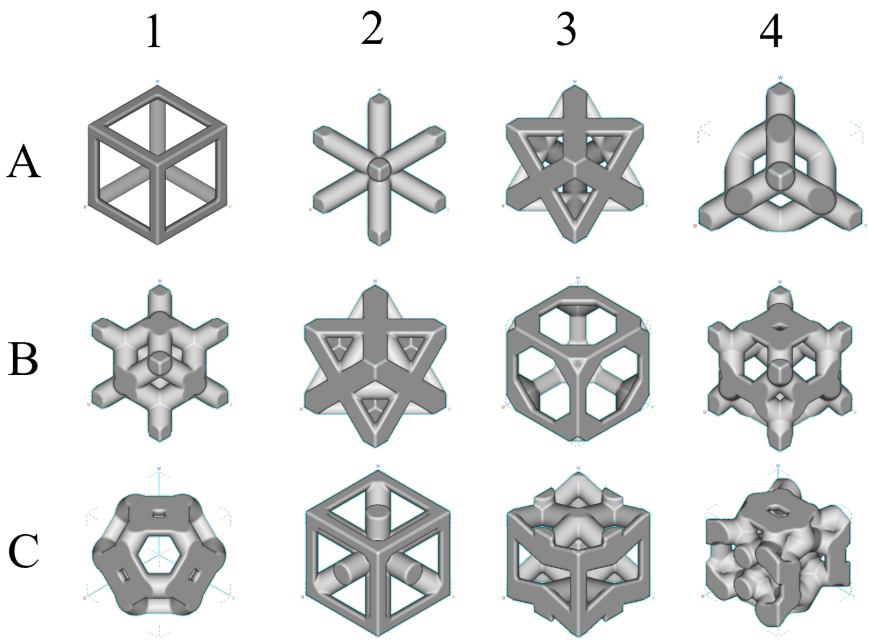


Figure 3.8: Example lattice unit cells, defined in Table 3.3

Table 3.3: Unit cell names, see Figure 3.8

Position	Unit Cell
1A	Simple cubic
2A	Body centered cubic (BCC)
3A	Face centered cubic (FCC)
4A	Diamond
1B	Flourite
2B	Octet
3B	Truncated cube
4B	Truncated octahedron
1C	Kelvin cell
2C	Iso truss
3C	Re-entrant
4C	Weaire-Phelan

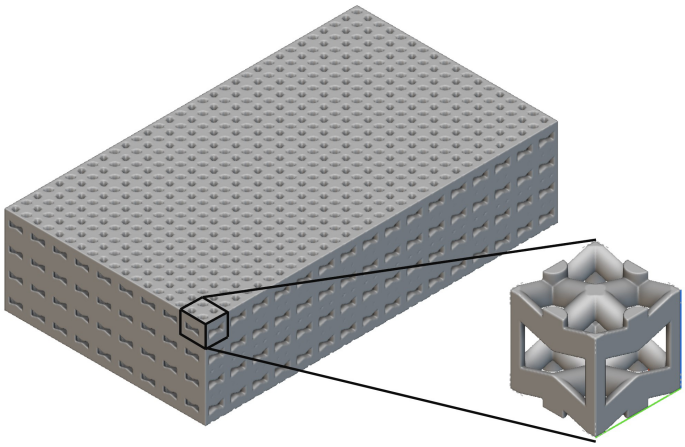


Figure 3.9: Modeled re-entrant lattice structure.

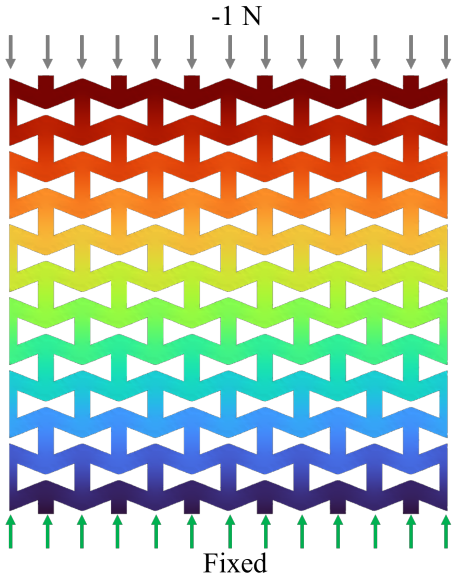


Figure 3.10: Example lattice stiffness conductivity simulation, boundary conditions shown.



Figure 3.11: Example lattice thermal conductivity simulation, boundary conditions shown.

Table 3.4: Select simulation results for Inconel lattices.

Cell Type	Thickness (mm)	Stiffness (N/m)	Conductivity (W/mK)
BCC	3	2.20×10^7	2.70
Diamond	3	3.30×10^7	4.70
FCC	3	2.90×10^8	7.84
Flourite	3	7.80×10^7	7.58
Gyroid	1	6.14×10^8	9.12
IsoTruss	2	1.06×10^9	4.61
Kelvin Cell	3	6.08×10^8	3.99
Octet	3	1.32×10^9	5.69
Re-Entrant	3	1.66×10^8	3.28
Re-entrant honeycomb	2	2.21×10^8	4.95
Simple Cubic	3	8.00×10^7	6.48
Truncated Cube	3	2.36×10^8	6.82
Truncated Octahedron	3	9.18×10^8	4.58
Voroni	1	4.07×10^8	7.70

After evaluating the simulation results, a re-entrant type unit cell was chosen for the final design, see Figure 3.8 cell C2. Results showed that it provided the best combination of stiffness and thermal conductivity. The exact specifications of the final design are proprietary to Oak Ridge National Laboratory under provisional patent USPTO 63545761, an example design is shown in Figure 3.9. The final component was printed out of Inconel 718 on a Concept Laser X-Line powder bed fusion machine, shown in Figure 3.12. Additive manufacturing enabled the lattice geometry to be manufactured, and affected the material properties. Components made using AM generally have higher defect counts, voids, inclusions, and grain boundaries, which can change material properties like thermal conductivity. The geometry and the manufacturing process were both selected to maximize the thermal resistance

The printed thermal insulator was removed from the base plate using wire electrical discharge machining (EDM). The top and bottom surfaces were machined and clearance holes drilled for mounting to the dynamometer platform. A small notch was ground into the bottom and top surfaces for a thermocouple to lay. All other surfaces were left in the as printed condition.

The final elevated cutting force measurement system has the following components, listed bottom to top: stainless steel CMD with air cooling, G-7 glass-silicone laminate, 2024 aluminum sheet, Inconel lattice, heating element, and workpiece, all through bolted with two $\frac{1}{4}$-20 A286 fasteners torqued to 20N/m. A286 was chosen for its high strength and continuous service limit of 540°C [56]. The assembly is shown in Figure 3.13 and a component breakdown is shown in Figure 3.14.

Convective cooling was added to further reduce the flexure platform temperature. The air inlet is a $\frac{1}{4}$ inch inner diameter tube with 40psi of pressure and flow rate of approximately 5.5 cfm(cubic feet per minute). Compressed air enters the bottom of the dynamometer and exits at the top through the space between the platform and body. The exiting air cools the aluminum plate, which also acts as a chip guard for the capacitance gauge. The air cooled plate lowers the temperature at the bottom of the Inconel spacer enough to use a G-7 laminate, which has high stiffness and low thermal conductivity, but low maximum temperature limit of 220°C. Type N special

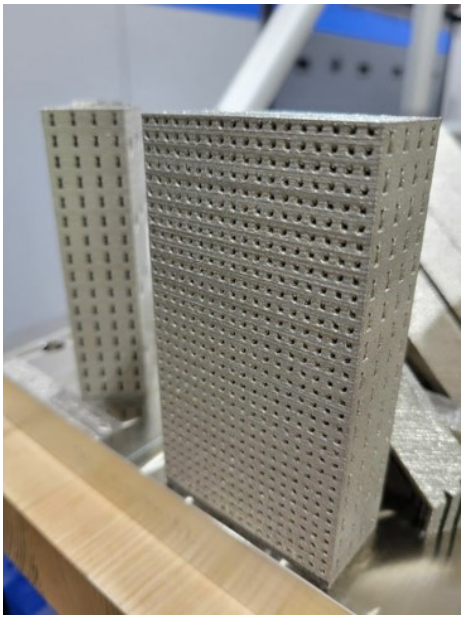


Figure 3.12: As printed Inconel lattice structure.

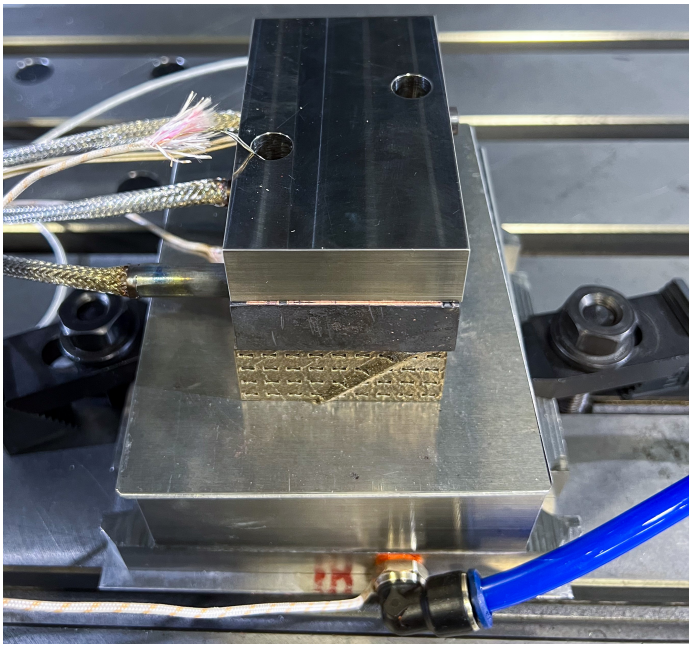


Figure 3.13: Elevated temperature cutting force dynamometer.

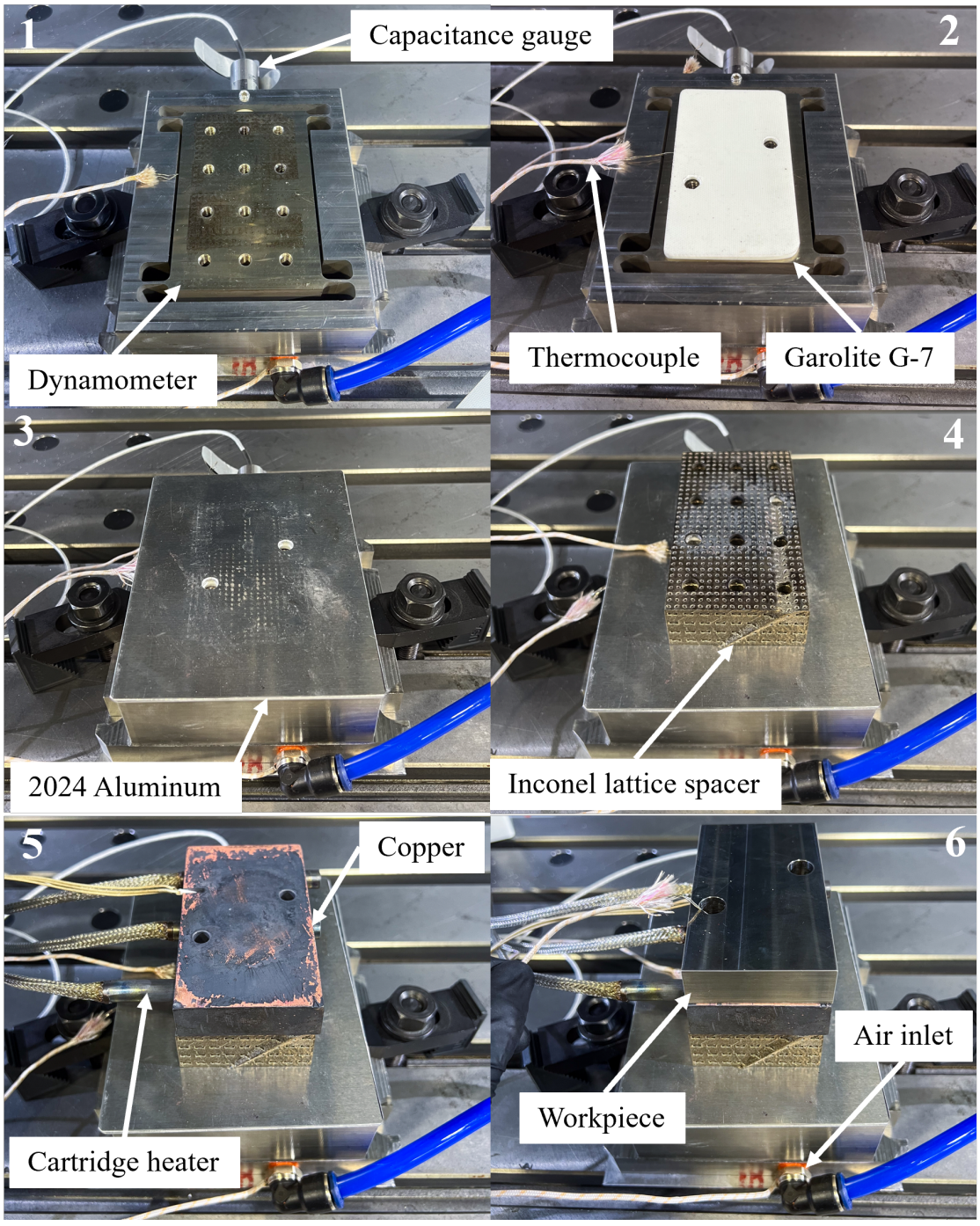


Figure 3.14: Elevated temperature cutting force dynamometer assembly.

limits of error (SLE) thermocouples are located on the bottom of the flexure platform, at the interface of the G-7 and top of the platform, the bottom of the Inconel spacer, the interface between the workpiece and heater, and the top of the workpiece. The capacitance gauge is secured to the dynamometer body with a set screw. Shims were used to reduce the clearance between the capacitance gauge body and mounting bore and to protect it from the set screw. The dynamometer body was secured to the machine table using four toe clamps and $\frac{1}{2}$-13 studs.

3.2 Measurement

3.2.1 Materials and equipment

$$k = \frac{F}{\Delta x} \tag{3.9}$$

An overview of the experimental setup is shown in figure 3.15. Three basic quantities were measured: temperature, cutting force, and tool wear. Workpiece temperature was controlled with a Chromalox intelliTRACE ITC controller using the onboard PID and a Class A 3 wire 100Ω RTD. The workpiece and dynamometer temperatures were measured with SLE type N thermocouples and a MadgeTech TCTempX series data logger sampling at 1Hz, and a FLIR A70 thermal camera. Type N thermocouples were chosen over the more common type K for their high temperature stability and resistance to oxidation. A thermocouple at the workpiece surface was used to calibrate the thermal camera over the range of workpiece temperatures, example image show in Figure 3.16, and determine the appropriate PID controller set points. Calibration over a range of temperatures was required because emissivity changes with temperature and surface condition. The thermocouple was removed prior to each group of cutting tests and the workpiece temperature was measured using the infrared (IR) camera. Tool wear was monitored with a Dino-Lite digital optical microscope. Images of the insert flank surface were taken and the flank wear width was measured using a scaled image. Cutting tests were conducted on a Haas VF-5 three axis vertical milling machine.

Table 3.5: Instrumentation and associated measurement uncertainty.

Instrument	Type	Uncertainty(±)	Temperature (°C)
Thermocouple	N SLE	2.0°C [59]	500
RTD	Class A 3 wire 100Ω	0.95°C	400
IR camera	FLIR A70	2% [60]	20-1000
Capacitance gauge	Lion Precision C18-13	420nm	20



Figure 3.15: Measurement setup. 1) Capacitance gauge amplifier. 2)Thermocouple data logger. 3) PID temperature controller. 4) Digital microscope. 5) Infrared camera. 6) Constant elevated temperature cutting force dynamometer.

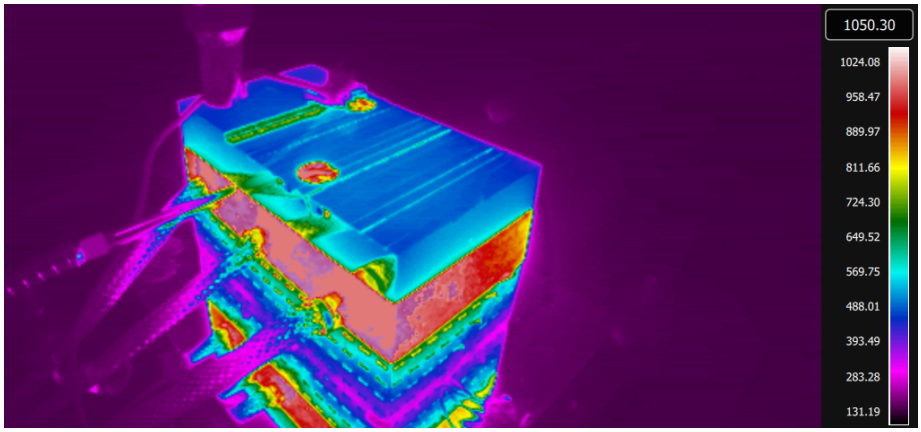


Figure 3.16: Infrared thermal image calibrated with thermocouple.

Materials for this study were chosen from alloys that meet the following criteria: commonly used in additive manufacturing, have well known material properties, available in wrought and wire or powder form, and have poor machinability. Materials that harden or strengthen in the temperature range of interest were excluded, such as precipitation-hardening 17-4 stainless.

Ti-6Al-4V is widely used in the aerospace, marine, and power generation industries for its high specific strength and corrosion resistance. Over 70% of all alloy grades melted are a sub-grade of Ti-6Al-4V [57]. It can be difficult to machine due to its low thermal conductivity, high chemical affinity for tool materials, and abrasive secondary phases [31]. Ti-6Al-4V is an excellent candidate for hybrid manufacturing because of high material and machining costs when using conventional strategies. Prior research has found an increase in tool life at elevated temperatures when machining Ti-6Al-4V [31, 58].

3.2.2 Experimental procedure

The dynamometer was aligned to the machine with the flexible direction oriented along the machine Y axis and secured to the table with four toe clamps. The capacitance gauge was installed, shimmed, and secured at a distance within its working range, and the charge amplifier was grounded and bolted to the machine table. A filtered air line with 40psi pressure was connected to the base of the dynamometer. Two adjustable magnetic clamps were used to hold the optical microscope and thermal camera. Simultaneous use of the capacitance gauge and thermocouples required the use of two computers with different paths to ground. The dynamometer was assembled as shown in Figure 3.14. Each time a workpiece was changed, the clamping bolts were torqued to 20N/m, 125µm of material was removed from the top surface, and a radial cut of 250µm was completed to ensure the alignment of the workpiece surface to the machine axis. The spindle was warmed up for a minimum of 5 minutes before each round of testing. A 12.7mm diameter single tooth indexable endmill with a S40T (CVD TiCrN + Al2O3+TiN) coated carbide insert was used in each test.

For every temperature the following procedure was followed:

1. The temperature was allowed to settle for a minimum of three oscillations at the set point.

2. The top face was machined at $Z0.0$.

3. The FRF was measured.

4. A cleanup pass was taken at the last cut location at an additional 50µm Z depth.

5. A cutting test at a RDOC of 2.54mm and ADOC of 2mm was completed with three feed rates {50, 75, and 100}$\frac{\mu m}{tooth}$

6. A cleanup pass was taken at the last cut location at an additional 50µm Z depth.

7. A cutting test at a RDOC of 2.54mm and ADOC of 2mm was completed with three feed rates {50, 75, and 100}$\frac{\mu m}{tooth}$

8. Steps 4-7 were repeated a total of three times.

9. A image of the cutting insert flank face was recorded and measured for flank wear. The insert was replaced when the flank wear width exceeded 350µm [61].

Data was collected for both the X and Y directions, at six temperatures {20, 100, 200, 300, 400, and 500}°C, five feed rates {50, 75, 100, 125, and 150}µm and three repeats. A summary of the cutting parameters and cutting tests are shown in Table 3.6 and Table 3.7 respectively. An example test cut is shown in Figure 3.17.

Re-facing the workpiece after each temperature change eliminated change in chip area due to thermal expansion. In the absence of this step, the total change in axial depth of cut was 0.5mm, or 25% of the commanded value, as the workpiece

Table 3.6: Summary of cutting parameters.

Tool Diameter	⌀12.7 mm
Cutting teeth	1
Axial depth	2.0 mm
Radial depth	2.54 mm
Feed per rev	50µm-150µm
Spindle speed	1100 rpm

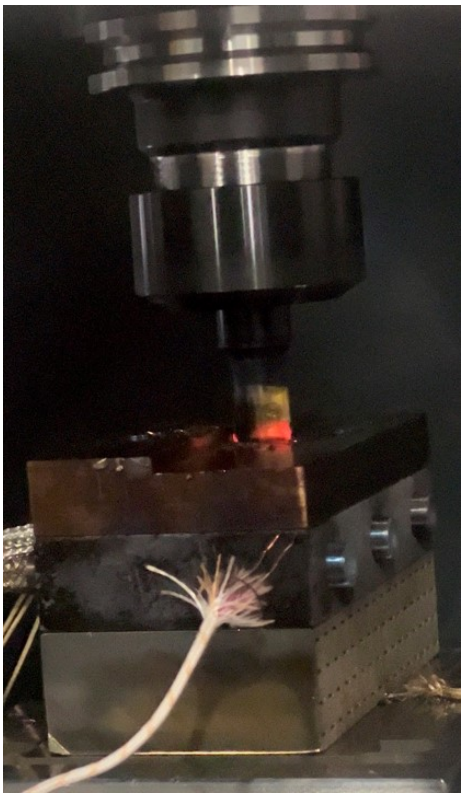


Figure 3.17: Cutting test at 400°C in Ti-6Al-4V.

Table 3.7: Summary of cutting tests, completed in both the X and Y directions.

Temperature (°C)	Feed rates (µm)	Number
20	50, 75, 100	1
20	125, 150	1
20	50, 75, 100	2
20	125, 150	2
20	50, 75, 100	3
20	125, 150	3
100	50, 75, 100	1
100	125, 150	1
100	50, 75, 100	2
100	125, 150	2
100	50, 75, 100	3
100	125, 150	3
200	50, 75, 100	1
200	125, 150	1
200	50, 75, 100	2
200	125, 150	2
200	50, 75, 100	3
200	125, 150	3
300	50, 75, 100	1
300	125, 150	1
300	50, 75, 100	2
300	125, 150	2
300	50, 75, 100	3
300	125, 150	3
400	50, 75, 100	1
400	125, 150	1
400	50, 75, 100	2
400	125, 150	2
400	50, 75, 100	3
400	125, 150	3
500	50, 75, 100	1
500	125, 150	1
500	50, 75, 100	2
500	125, 150	2
500	50, 75, 100	3
500	125, 150	3

temperature varied between 20°C and 500°C. The cleanup passes removed the influence of the previous cutting test and ensured the bottom face of the tool was not engaged in the workpiece. The distances of each feed rate in the cut was set to result in the same time in the cut for all feed rates. Cutting tests were always conducted in order of increasing temperature.

Displacement data was collected using a Lion Precision C18-13 capacitance gauge, charge amplifier, high-bandwidth data acquisition (DAQ), and SpinScope, a signal processing software, at a sampling frequency of 50kHz and sensitivity of 12.5V/mm. The time domain data in the SpinScope format was converted into a Matlab file for processing. The system dynamics were measured using an instrumented hammer, capacitance gauge, DAQ, and TXF software, with a measurement bandwidth of 5kHz. The real and imaginary parts of the FRF were exported as a Matlab file for processing.

3.2.3 Data processing

For each temperature and test number data set, the following process was completed:

1. The time domain displacement data for a pair of tests, $\{50,\ 75,\ \text{and}\ 100\}\frac{\mu m}{tooth}$ and $\{125\ \text{and}\ 150\}\frac{\mu m}{tooth}$, were imported into Matlab.

2. The start and end of the data was truncated by removing points less than 5x the average capacitance gauge noise signal, determined by the mean of the first 10,00 data points in the file.

3. For each feed rate an approximately 10 second section was selected, capturing roughly 180 tooth impacts, shown in Figure 3.18.

4. The parsed displacement and time vector for each of the five feed rates was saved as a new data set. The parsed displacement data for a single set of five feed rates is shown overlaid in Figure 3.19.

The dynamometer FRF data was imported as the real and imaginary parts. Modal peak picking was used to model the FRF as a single degree of freedom system [13]. The frequency of the imaginary peak, 1, the amplitude of the imaginary peak, A, and the frequencies of the positive and negative real peaks, 2 and 3, as shown in Figure 3.20, were used to calculate the natural frequency ω_{n1}, and the modal parameters k_q (modal stiffness), c_q (modal damping ratio), and m_q modal mass. The modal fitting parameters and SDOF FRF fit are shown in Equations 3.10 and 3.11 and a sample fit is show in Figure 3.21.

$$\zeta_q = \frac{\omega_3 - \omega_2}{2\omega_{n1}} \qquad k_q = \frac{-1}{2\zeta_q A} \qquad m_q = \frac{k_q}{w_{n1}^2} \qquad c_q = 2\zeta_q\sqrt{k_q m_q} \tag{3.10}$$

$$FRF_{fit} = \frac{-1}{-m_q\omega^2 + 1ic_q\omega + k_q} \tag{3.11}$$

A single-pole infinite impulse response (IIR) lowpass filter with a passband frequency range of less than 650Hz and stopband frequency range of greater than 1000Hz was convolved with the inverted FRF, show in Figure 3.22. Note how as the frequency increases the inverted FRF magnitude increases to infinity without the low pass filter. The process to convert from time domain displacement to time domain force is summarized by Equations 3.1 to 3.3 in Section 3.1.1. The filtered and inverted FRF was convolved with the displacement signal and converted to time domain force using the inverse fast Fourier transform (FFT).

The DC offset was calculated as the mean of the signal between impulses and removed from the force data. Cutting force peaks with spacing equal to the tooth passing frequency were identified and recorded as the peak force. The mean force was calculated as the average of the force over one revolution of the cutter. The mean of the three data sets was calculated for each temperature and feed rate combination for the peak and mean force values. The results are reported in Chapter 4.

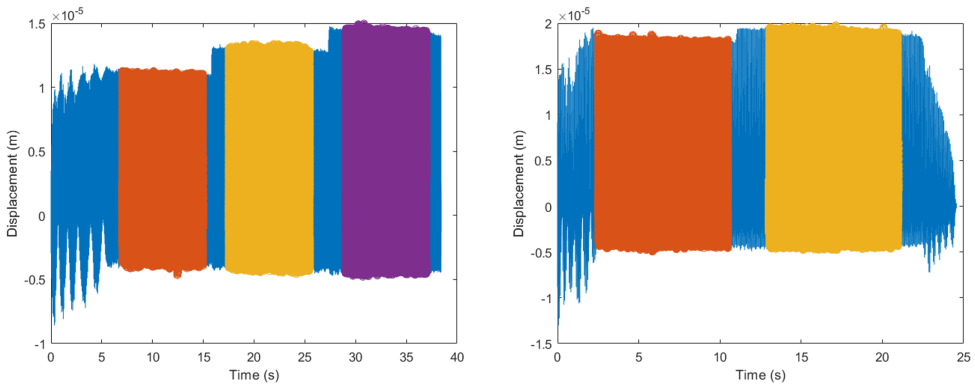


Figure 3.18: Selection of cutting data. Blue is the trimmed displacement data, colored selections represent different feed rates.

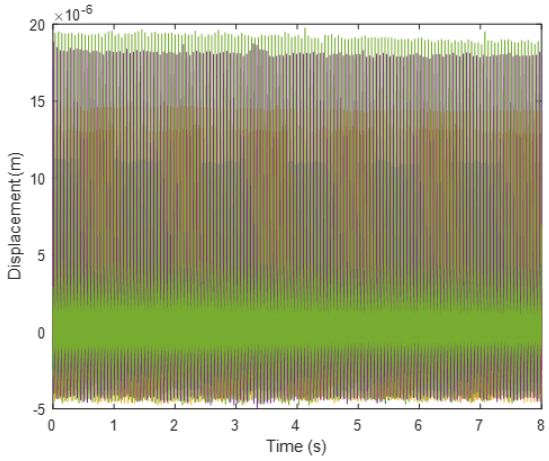


Figure 3.19: Overlaid displacement data for one set of cutting tests, five feed rates.

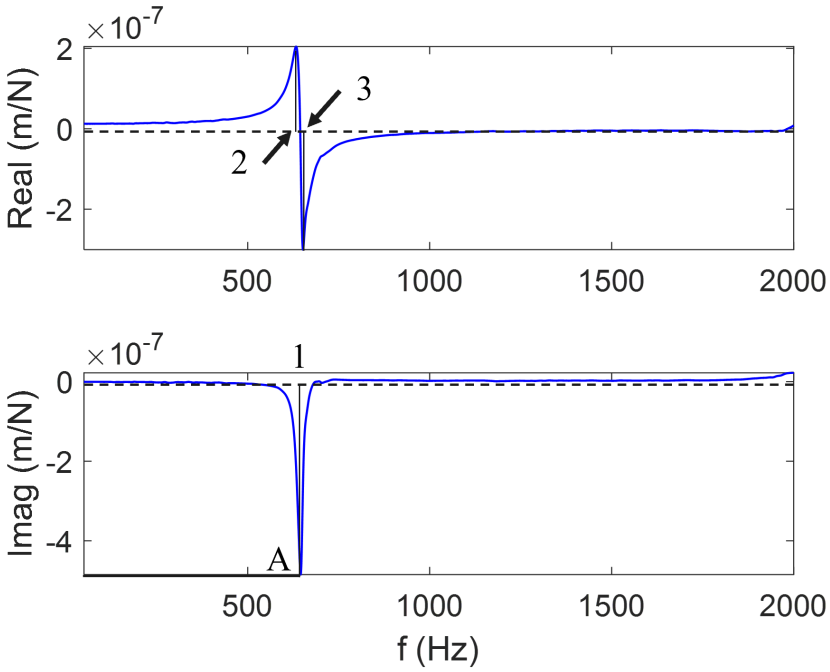


Figure 3.20: Peak picking of measured FRF.

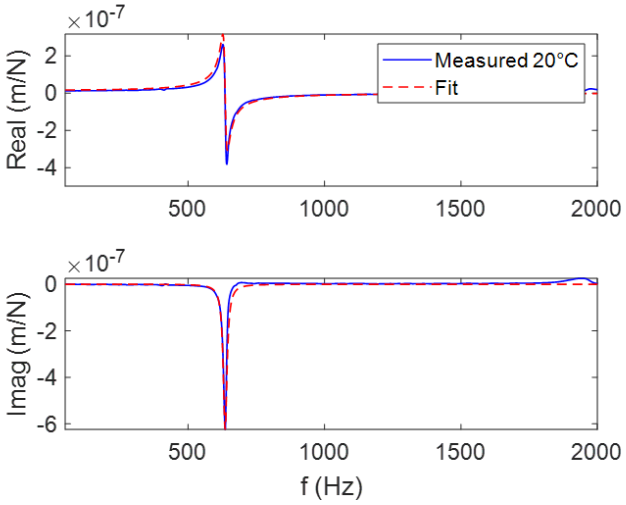


Figure 3.21: SDOF FRF measurement and fit

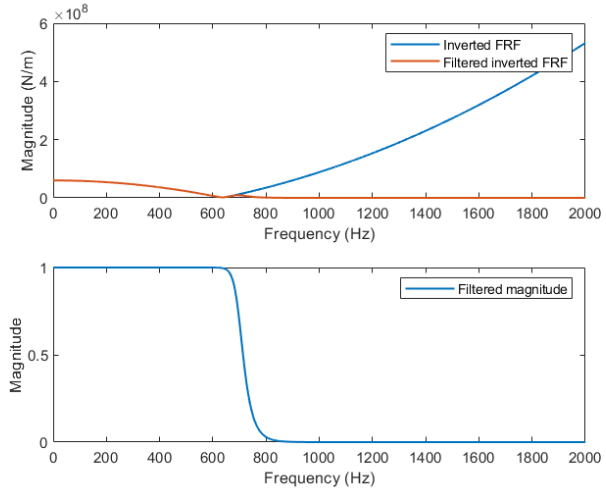


Figure 3.22: (Top) Inverse FRF and filtered inverse FRF. (Bottom) filter.

Chapter 4

Results and Discussion

4.1 Elevated temperature force dynamometer

The design criteria for the elevated temperature cutting force dynamometer were to 1) hold a workpiece at a maximum temperature of 500°C, 2) reduce the uncertainty in the workpiece temperature measurement, 3) retain sufficient stiffness to complete cutting tests in Ti-6Al-V4, and 4) minimize the change in the stiffness and natural frequency. Each of the design goals was met.

Temperature Uncertainty

The largest source of temperature measurement uncertainty in thermally assisted machining TEM is the large thermal gradients from the spot heat source. The two most common instruments for measuring workpiece temperature are thermocouples and infrared thermography (IR). Using a thermocouple where there is a large thermal gradient and rapidly changing temperatures adds to the measurement uncertainty. Thermocouples lag the system they are measuring as heat is transferred to the junction and are calibrated assuming the junction is at a uniform temperature. This uncertainty can be minimized by ensuring the junction does not experience thermal gradients.

In IR thermography, emissivity is typically the largest contributor to uncertainty, followed by uncertainty in measured spectral radiance. The emissivity of a body is the ratio of the total emitted radiation from a real surface to the radiation emitted by a perfect black body at the same temperature. The value depends on the material, surface finish, surface oxidation, and temperature, among other factors, see Figure 4.1. The square of the IR measurement error increases proportionally with the square of the temperature and in inverse proportion to the square of the emissivity. The emissivity from the center of a laser spot, for example, will have a different emissivity value than the bulk workpiece. Davies *et al.* and Lane *et al.* determined a combined standard uncertainty in temperature measurement in material removal processes of ± 52°C and ± 50.1°C respectively up to 850°C [48, 62]. In both cases, temperature measurement has a lower associated uncertainty at steady state conditions.

In this study the measuring target, the workpiece surface, was maintained at a constant temperature and surface condition, and the IR camera remained fixed relative to the workpiece. The emissivity at a particular temperature, material, and surface condition is constant. The temperature of the workpiece surface was measured using a type N thermocouple with an uncertainty of ± 1.1°C or 0.4% (whichever is greater). The emissivity was adjusted as the temperature increased and the surface oxidized to match the thermocouple value.

The standard deviation of the workpiece surface temperature over 10 minutes and 10 seconds, the average length of a single cutting test, is presented in Table 4.1, calculated using thermocouple data. The cutting forces and workpiece temperature are measured as an average over the length of a cutting test. Therefore the temperature variation over the length of cut adds to the uncertainty. The variability in workpiece temperature was calculated as two times the standard deviation (σ) values presented in Table 4.1. The combined standard uncertainty of the thermocouple, data logger, workpiece temperature variation, and IR camera is ± 10.27°C at 500°C. See Table 4.2 for full temperature range.

The target workpiece temperature of 500°C was achieved, see Figures 4.2 and 4.3, and maximum workpiece surface temperature of 640°C was observed. However, at

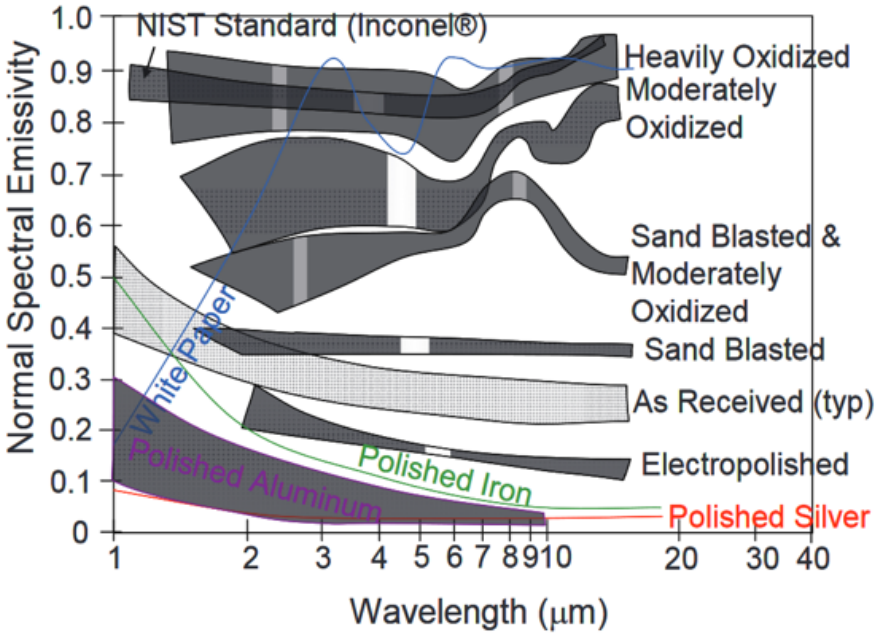


Figure 4.1: Spectral emissivity of various materials [62]

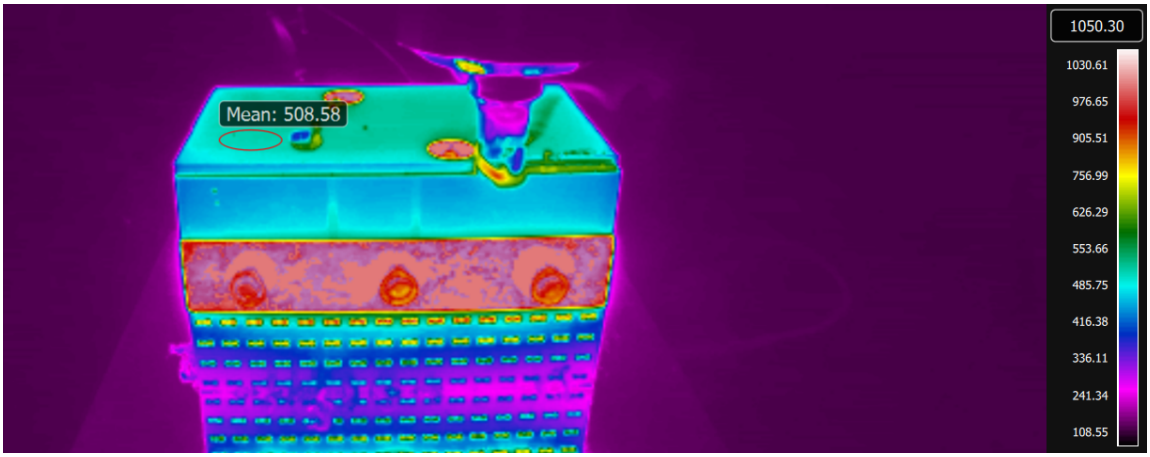


Figure 4.2: Calibrated IR image of 500°C cutting test.

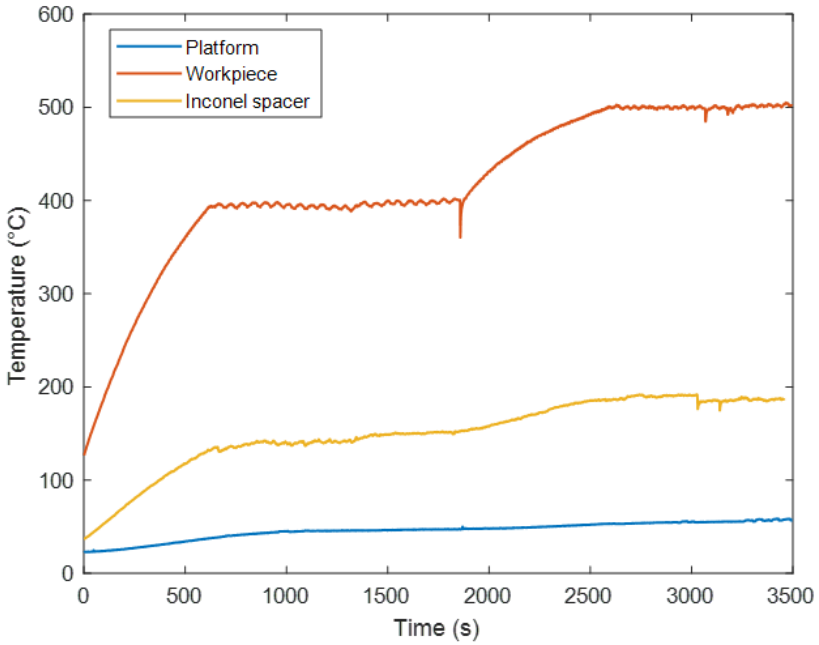


Figure 4.3: Temperature of the dynamometer platform, workpiece, and insulator up to a workpiece temperature of 500°C.

Table 4.1: Workpiece temperature standard deviation from steady state mean.

Temperature	Time (s)	σ (°C)
100	600	0.23
100	10	0.23
200	600	0.58
200	10	0.37
300	600	1.26
300	10	0.52
400	600	1.17
400	10	0.59
500	600	1.57
500	10	0.59

Table 4.2: Temperature combined measurement uncertainty.

Temperature (°C)	Uncertainty(±°C)
20	1.17
100	2.33
200	4.21
300	6.21
400	8.24
500	10.27

this temperature the service limit of the RTD and cartridge heaters is exceeded.

Dynamometer Variability

The dynamometer platform was successfully kept below 60°C with the workpiece at a temperature of at least 400°C for an hour, Figure 4.3. The maximum temperature reached was 58.7°C with an average temperature of 45.9°C. The effect of the convective cooling was tested and the results shown in Figure 4.4. The dynamometer platform started at a temperature of 47.6°C and rose to 80.2°C over 6 minutes after the air supply was shut off. A brief failure in the cooling system would cause damage to a traditional multi-force component dynamometer. The effect of the air cooling on the capacitance gauge was evaluated by measuring the noise signal with an without the air, see Table 4.3.

The FRF of the dynamometer was measured at the start of each new temperature. While evaluating the dynamometer, four sets of FRF measurements were completed. One set over the full range of workpiece temperatures is shown in Figure 4.5. All 24 FRFs are shown in Figure 4.6. The average change in natural frequency over the workpiece temperature range was -2.5% and the average change in stiffness was -4.51%, see Table 4.4. The mean standard deviation across all temperatures of the natural frequency and stiffness was 7.5Hz and 5.5×10^6N/m respectively. These values resulted from an approximately 40°C increase in the dynamometer platform temperature and 480°C increase in workpiece temperature. Some of the change in natural frequency is attributed to changing workpiece mass.

The change in Z height of the workpiece surface was measured as a function of temperature. From room temperature to 500°C, the surface height increased by 0.5mm, or 25% of the commanded ADOC. This change was from a stackup of materials of approximately 60mm. The change in ADOC and RDOC for parts made with hybrid manufacturing may be much greater, depending on the workpiece material and size, as thermal expansion increases linearly with temperature. The result of the thermal growth can be seen in Figure 4.7.

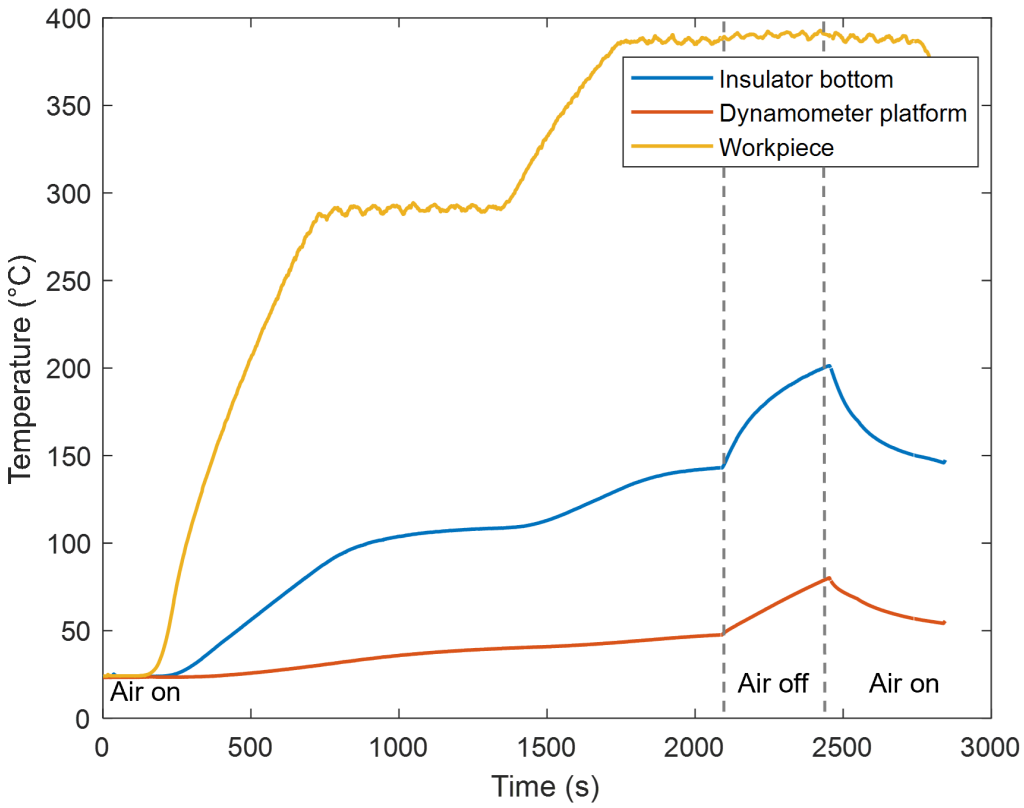


Figure 4.4: Testing the effect of the air cooling on the temperature of the dynamometer platform, workpiece, and insulator up to a workpiece temperature of 400°C.

Table 4.3: Average and standard deviation of capacitance gauge noise with convective cooling.

Condition	$\overline{x}$ (nm)	σ_x (nm)
Static	17.23	9.46
Air	18.68	11.23

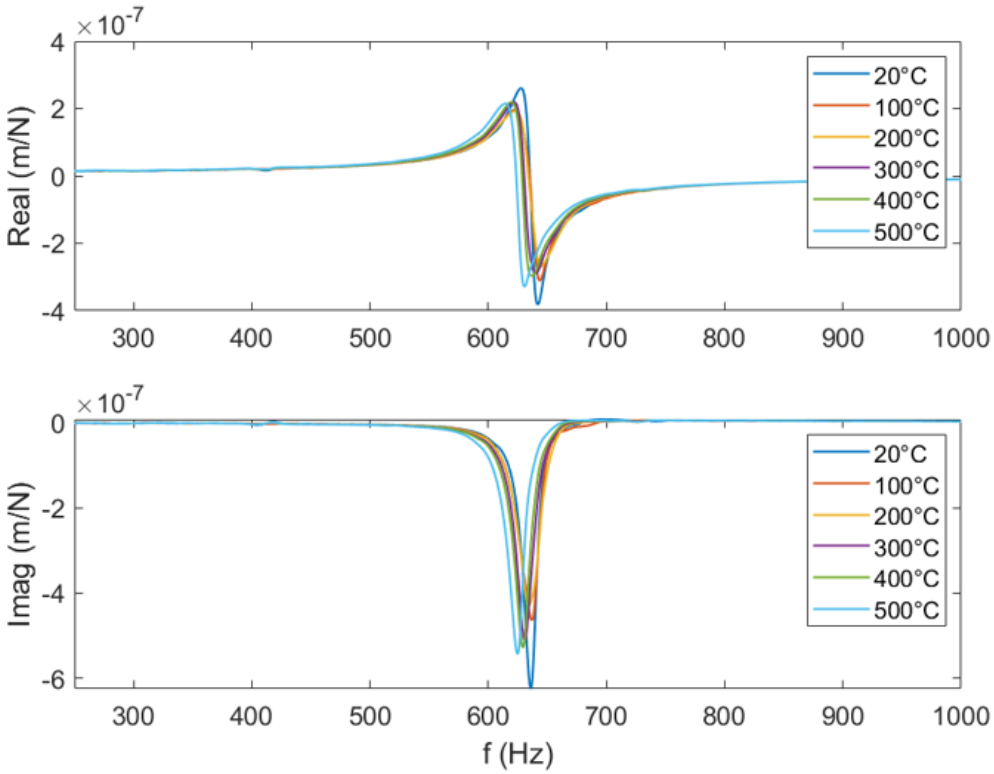


Figure 4.5: Frequency response of the constrained motion dynamometer with changing workpiece temperature over one set of cutting tests.

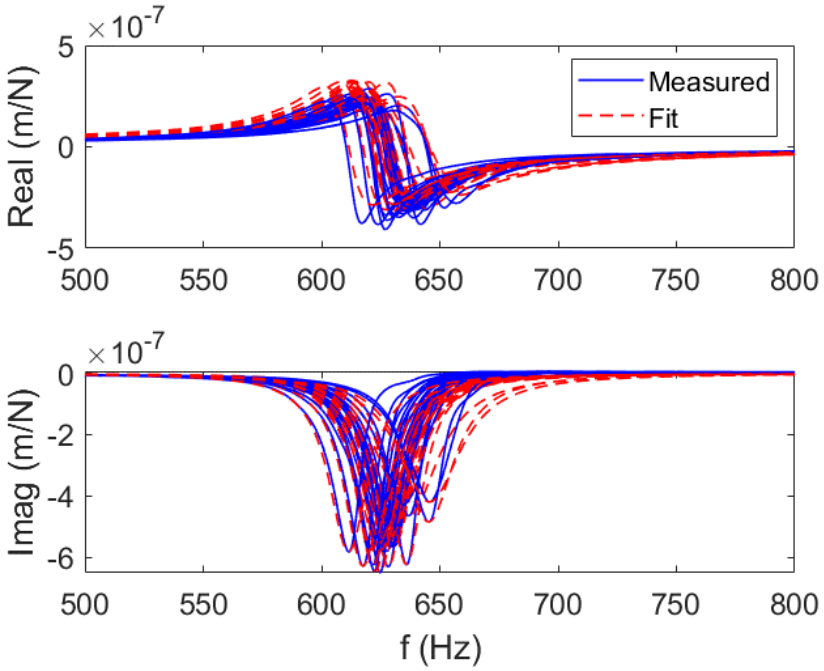


Figure 4.6: Plot of all measured and fitted dynamometer FRFs, four sets of tests at six temperatures.

Table 4.4: Average and standard deviation of natural frequency and modal stiffness at nominal workpiece temperatures. Four measurements were taken at each temperature.

Temperature (°C)	$\overline{f_n}$ (Hz)	σ_{fn} (Hz)	$\overline{k}$ ($\frac{\text{N}}{\text{m}}$)	σ_k ($\frac{\text{N}}{\text{m}}$)	Damping (%)
20	634.9	6.8	5.54×10^7	3.73×10^6	1.23
100	635.1	7.0	5.28×10^7	6.41×10^6	1.58
200	629.6	2.9	6.06×10^7	4.02×10^6	1.46
300	627.0	2.6	5.93×10^7	3.81×10^6	1.43
400	624.6	3.1	5.30×10^7	5.94×10^6	1.27
500	618.9	5.0	5.297	1.89×10^6	1.25
Mean	628.4	7.5	5.57×10^7	5.55×10^6	1.37

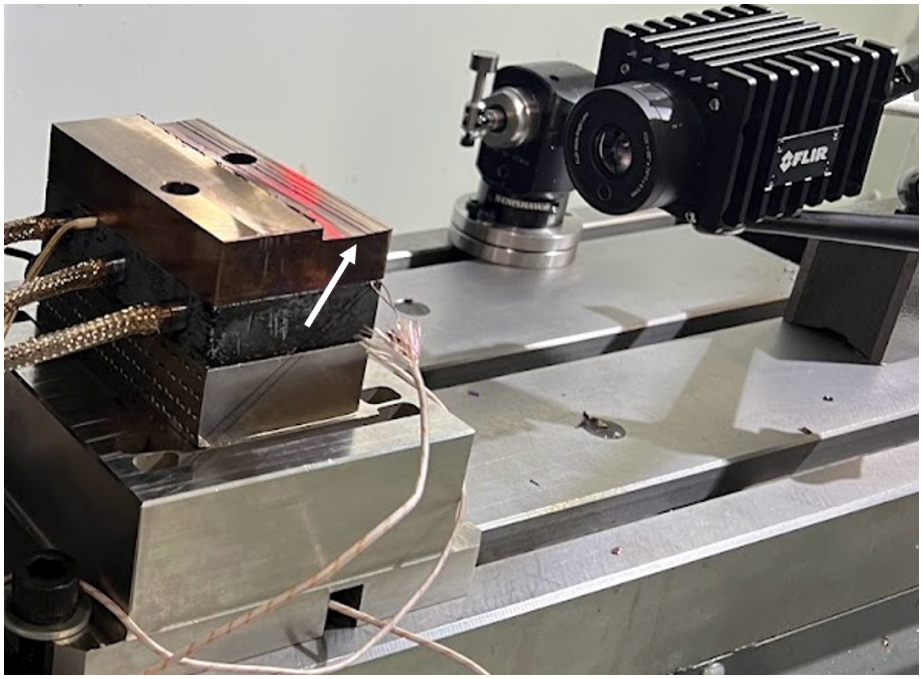


Figure 4.7: Workpiece cooled to room temperature after elevated temperature cutting. The staircase effect seen at the top of the workpiece and identified by the arrow is the result of thermal expansion.

4.2 Cutting force results

Displacement to force

The process to convert time domain displacement to cutting force is covered in detail in Section 3.1.1. A summary is presented here. A SDOF model was fit to the measured dynamometer FRF, the time domain displacement was converted to the frequency domain using the FFT, the frequency domain displacement was converted to frequency domain force using the filtered and inverted FRF, and the frequency domain force was converted back to the time domain using the inverse FFT. The mean and peak force was calculated for each temperature, feed rate, and test iteration, presented in Tables 4.5 (peak force) and 4.6 (mean force).

The force results for a single temperature and feed rate in the X and Y directions are shown in Figures 4.8 and 4.9 respectively. The individual tooth impacts over the cutting test are superimposed on each other. The force results for a all temperatures and a single feed rate are shown in Figures 4.10 and 4.11, with the results from each test superimposed on each other. Figure 4.12 shows force data from a free cooling cutting test, where the workpiece was heated to 500°C and allowed to cool. Cutting tests were taken at evenly spaced intervals until the workpiece reached 180°C. No compensation for ADOC was made. The peak and mean forces in the X direction are shown in Figures 4.13 and 4.14, and in the Y direction in Figures 4.15 and 4.16. The resultant cutting force is shown in Figure 4.17.

In all cases, constant temperature and constant feed, there was a significant initial decrease in the cutting force observed between 20°C and 100°C, followed by an increase above room temperature cutting force at 200°C, followed by a quasi-linear decrease in cutting force to a low at 500°C.

The increase in cutting force in the X direction at 500°C can be attributed to the material reaching a temperature at which the chips begin to adhere to the tool and back to the surface. This effect can be seen in Figure 4.18, where the chips were welded back onto the cutting surface after a conventional milling cut at 500°C.

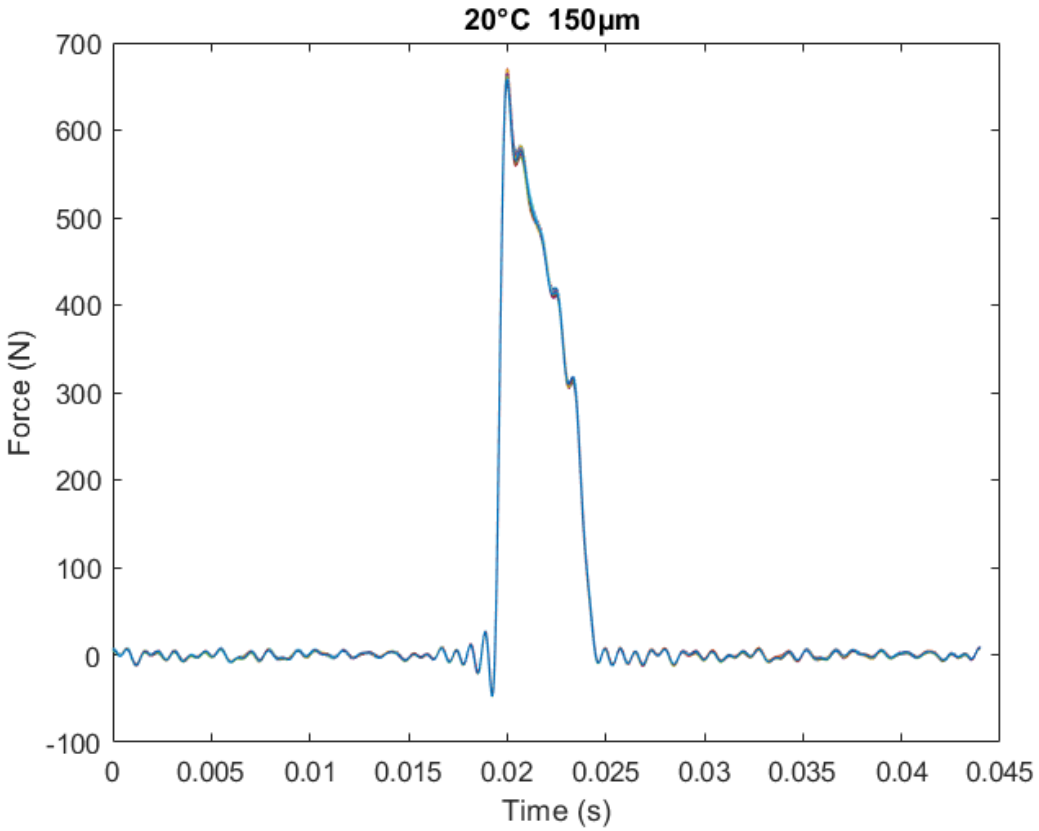


Figure 4.8: Y cutting force at 20°C and $150\frac{\mu m}{tooth}$. All tooth impacts are overlaid.

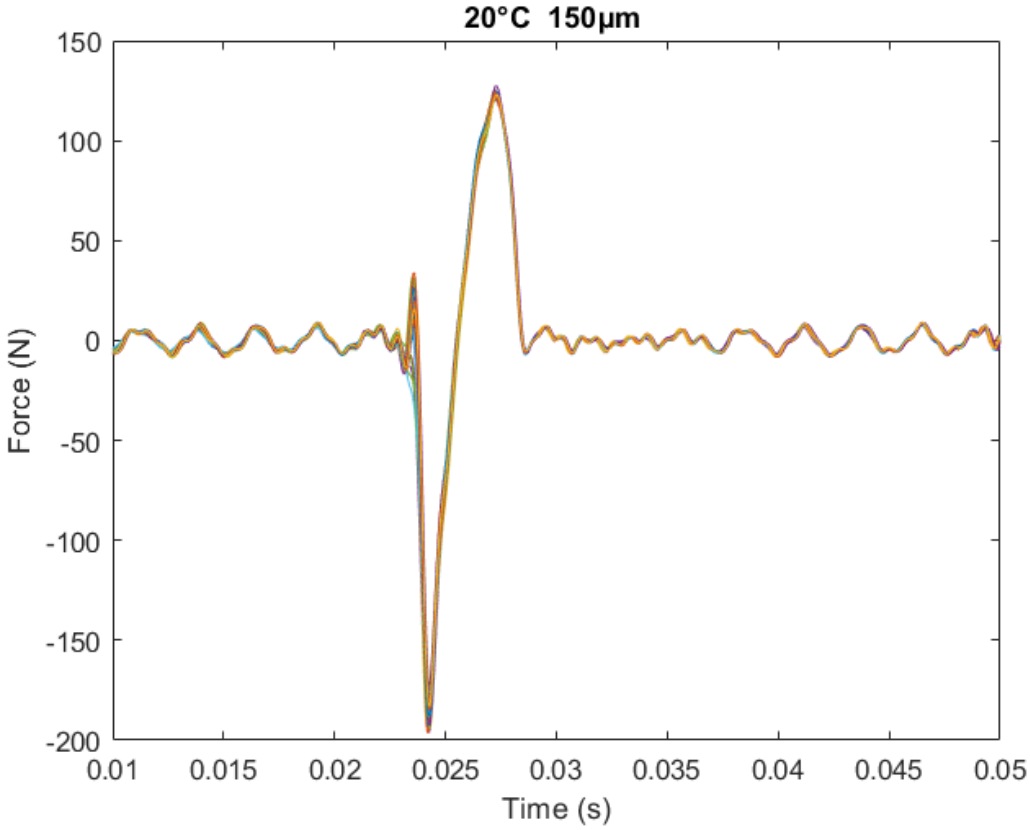


Figure 4.9: X cutting force at 20°C and 150$\frac{\mu m}{tooth}$. All tooth impacts are overlaid.

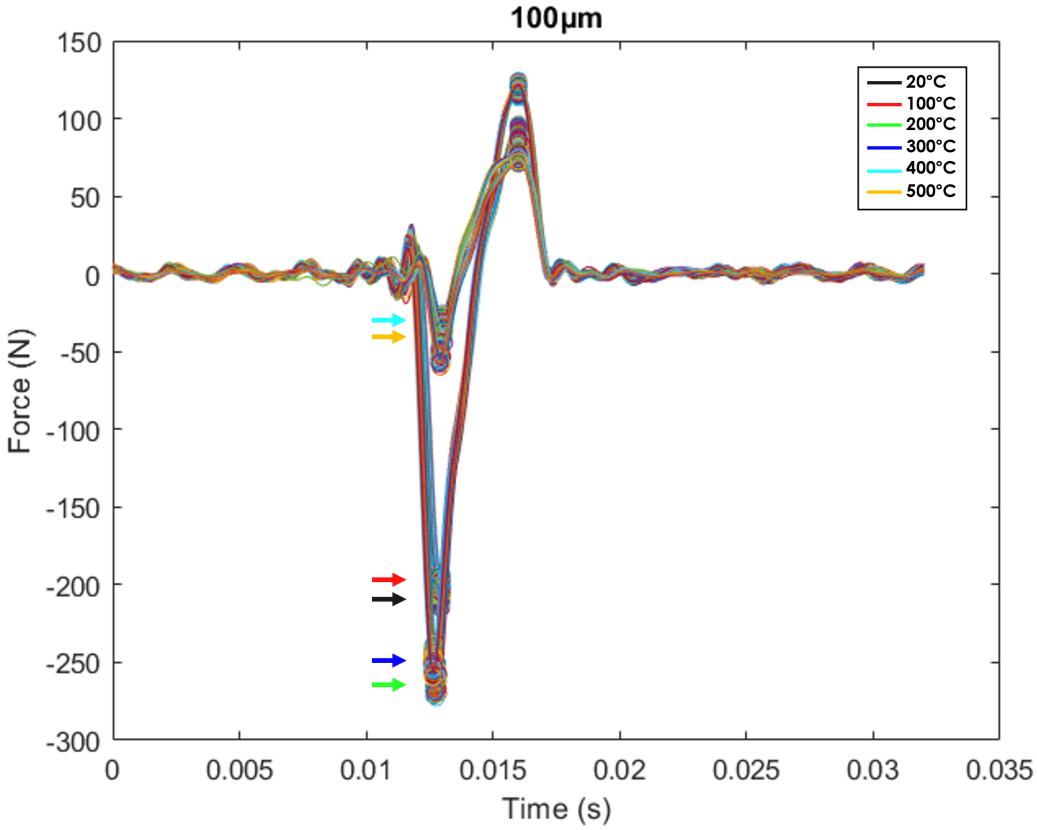


Figure 4.10: X cutting force at $100\frac{\mu m}{tooth}$ over six temperatures.

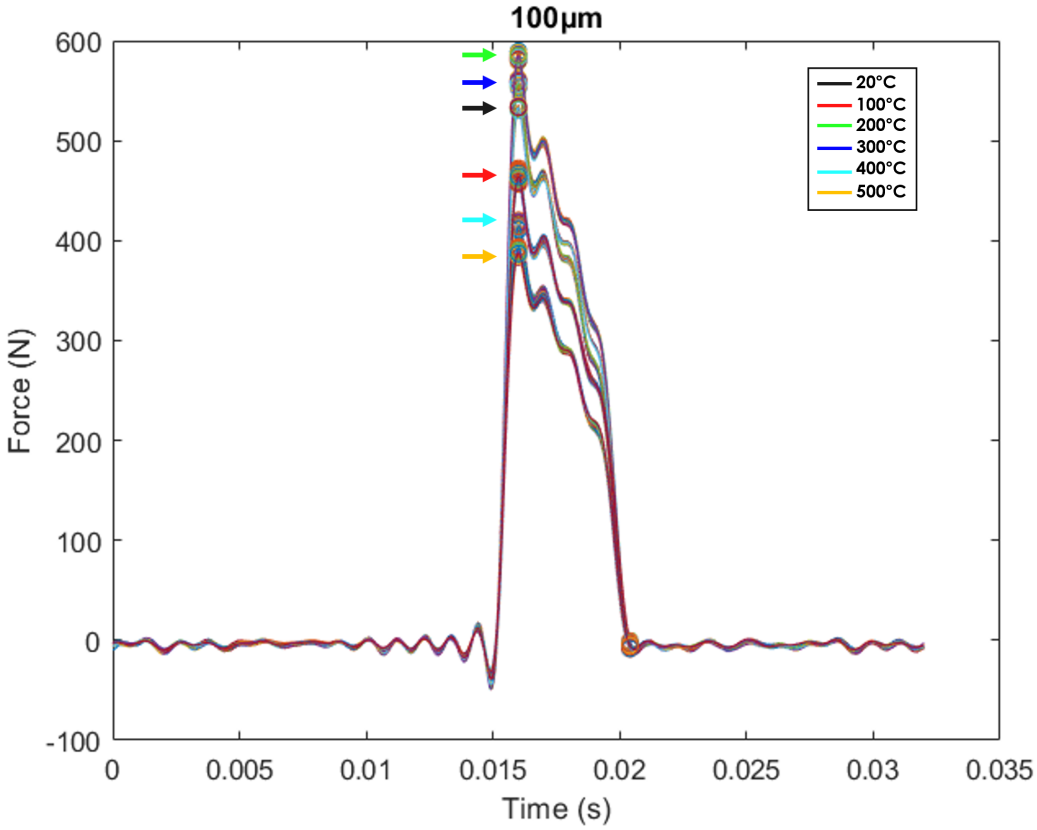


Figure 4.11: Y cutting force at $100\frac{\mu m}{tooth}$ over six temperatures.

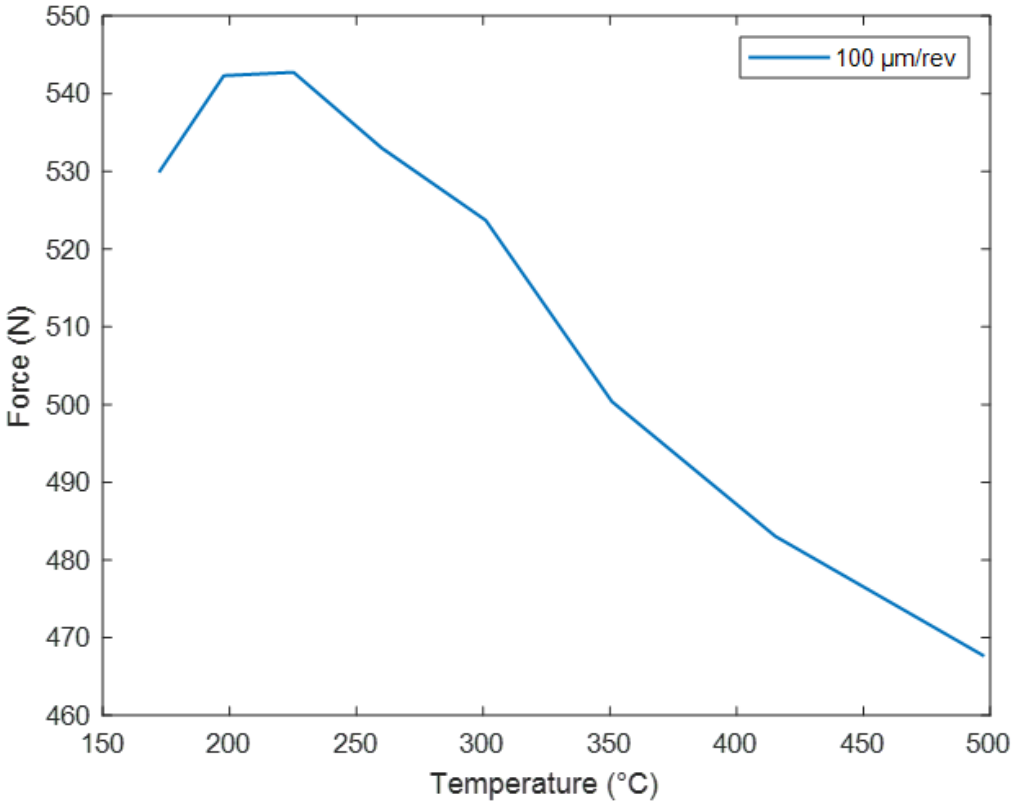


Figure 4.12: X direction forces with constant feed and free cooling.

Table 4.5: Average of the peak cutting force.

		Temperature (°C)					
		20	100	200	300	400	500
Axis	Feed rate (µm)	Cutting force (N)					
X	50	236.9	228.7	294.4	283.2	82.1	79.6
	75	229.4	220.5	279.6	263.4	65.1	67.1
	100	217.8	211.1	266.8	249.7	50.3	51.9
	125	206.7	196.3	233.8	214.6	36.1	28.4
	150	190.3	182.3	222.0	211.2	31.2	17.3
Y	50	413.3	327.9	470.3	438.1	377.3	321.7
	75	487.9	375.9	530.6	488.4	423.3	358.9
	100	538.1	414.1	579.6	532.1	461.7	384.8
	125	620.7	458.1	641.4	589.1	510.8	424.2
	150	658.4	487.9	687.6	630.3	550.1	460.7

Table 4.6: Average of the mean cutting force.

		Temperature (°C)					
		20	100	200	300	400	500
Axis	Feed rate (µm)	Cutting force (N)					
X	50	8.0	7.9	10.1	9.6	-1.4	-0.1
	75	5.7	5.8	7.4	6.5	-3.7	-2.0
	100	3.4	3.4	4.4	4.0	-5.9	-3.9
	125	0.5	0.7	0.0	-0.3	-8.0	-6.5
	150	-1.9	-1.3	-2.2	-2.0	-9.9	-8.2
Y	50	48.3	39.5	57.8	55.0	47.7	40.5
	75	53.9	43.5	62.8	59.2	51.7	43.7
	100	58.3	46.9	67.5	62.8	54.9	46.5
	125	67.5	49.1	73.7	67.8	59.1	49.8
	150	71.3	51.7	77.6	70.7	62.0	52.4

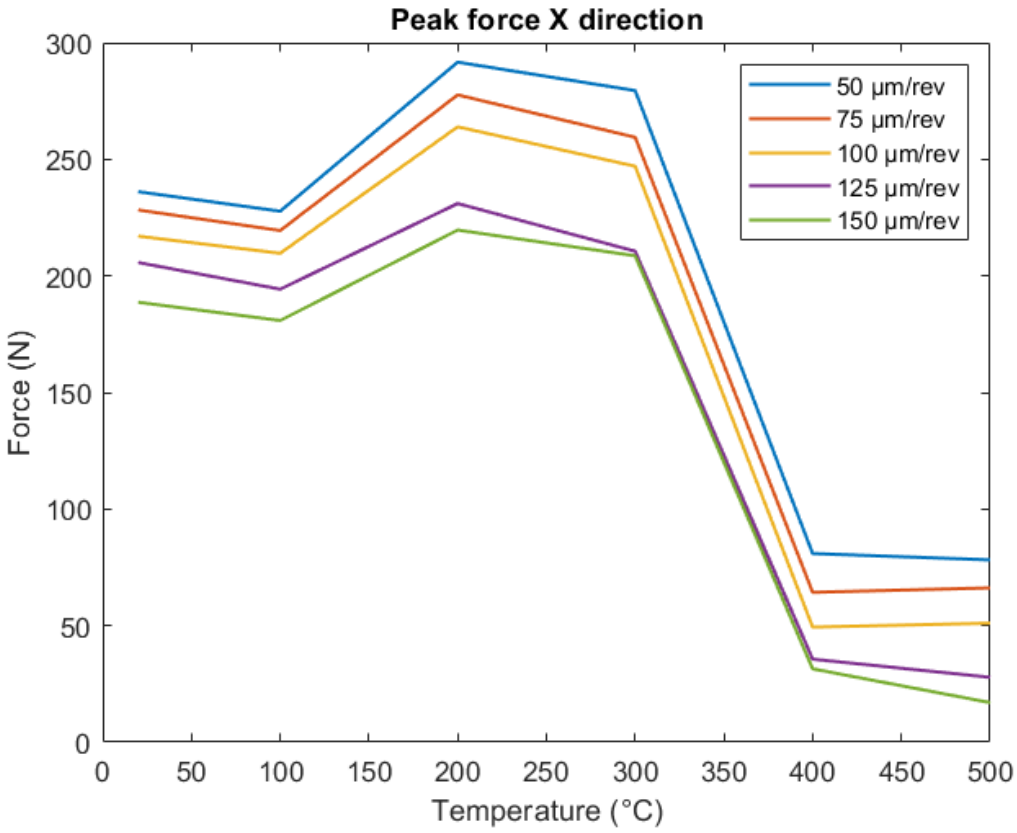


Figure 4.13: Peak force in X over a range of temperatures and feed rates in Ti-6Al-4V.

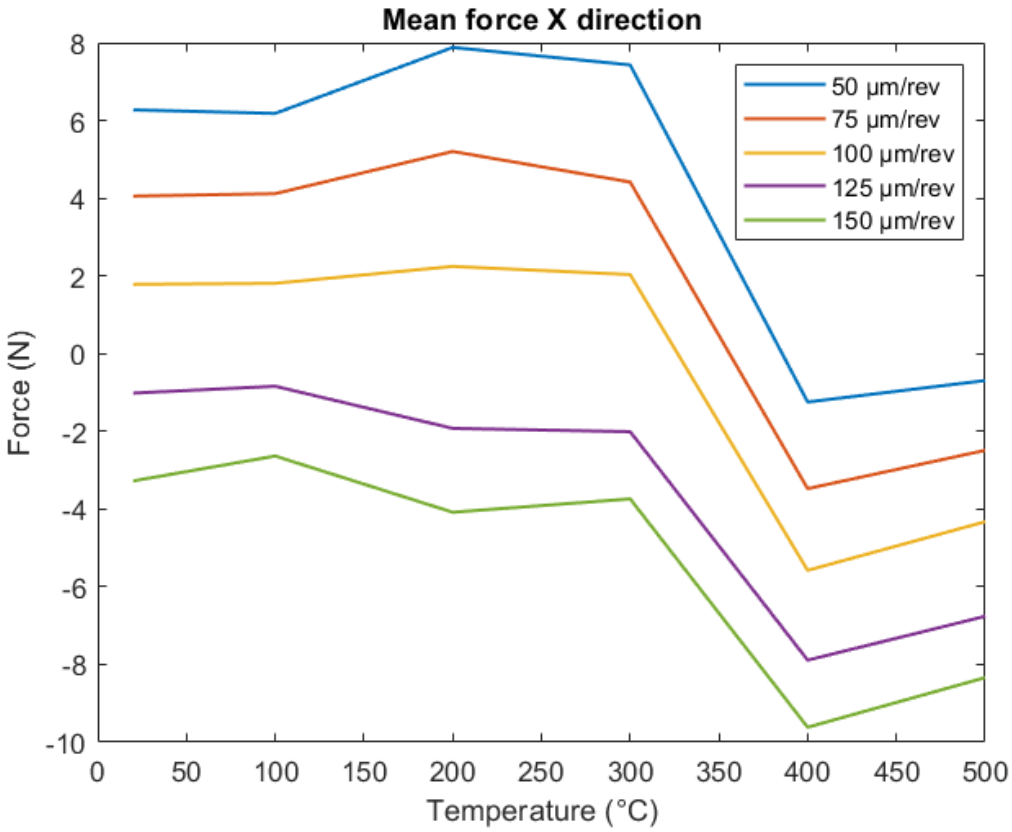


Figure 4.14: Mean force in X over a range of temperatures and feed rates in Ti-6Al-4V.

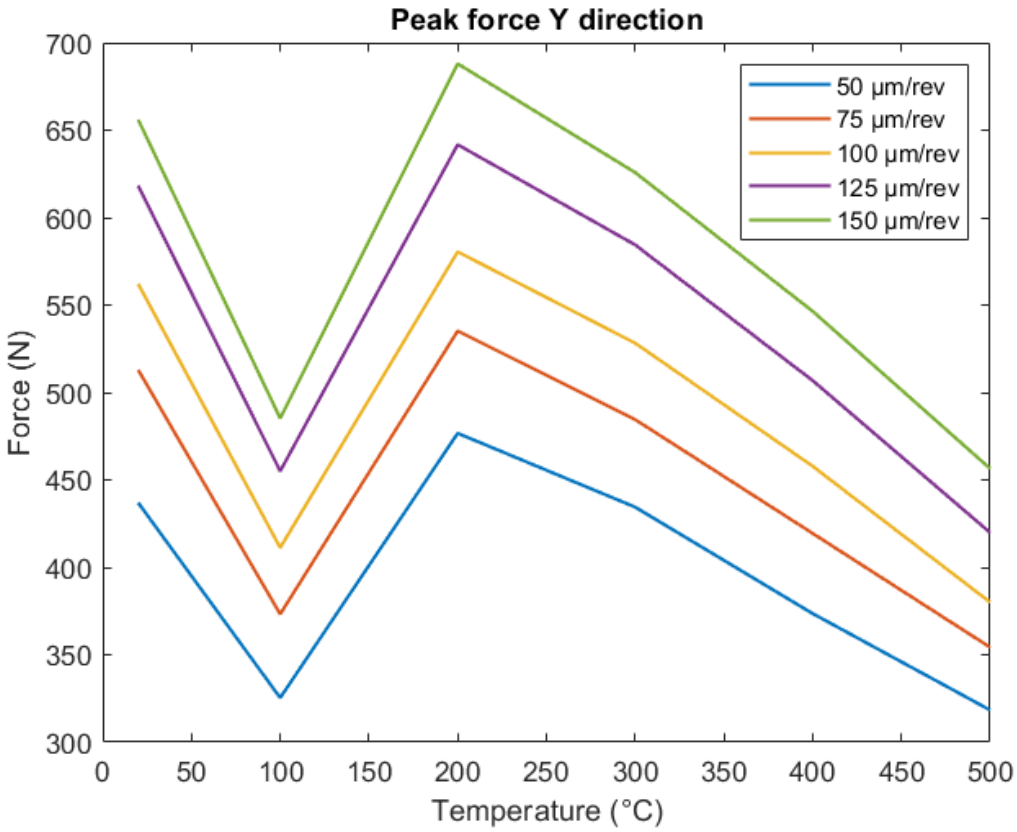


Figure 4.15: Peak force in Y over a range of temperatures and feed rates in Ti-6Al-4V.

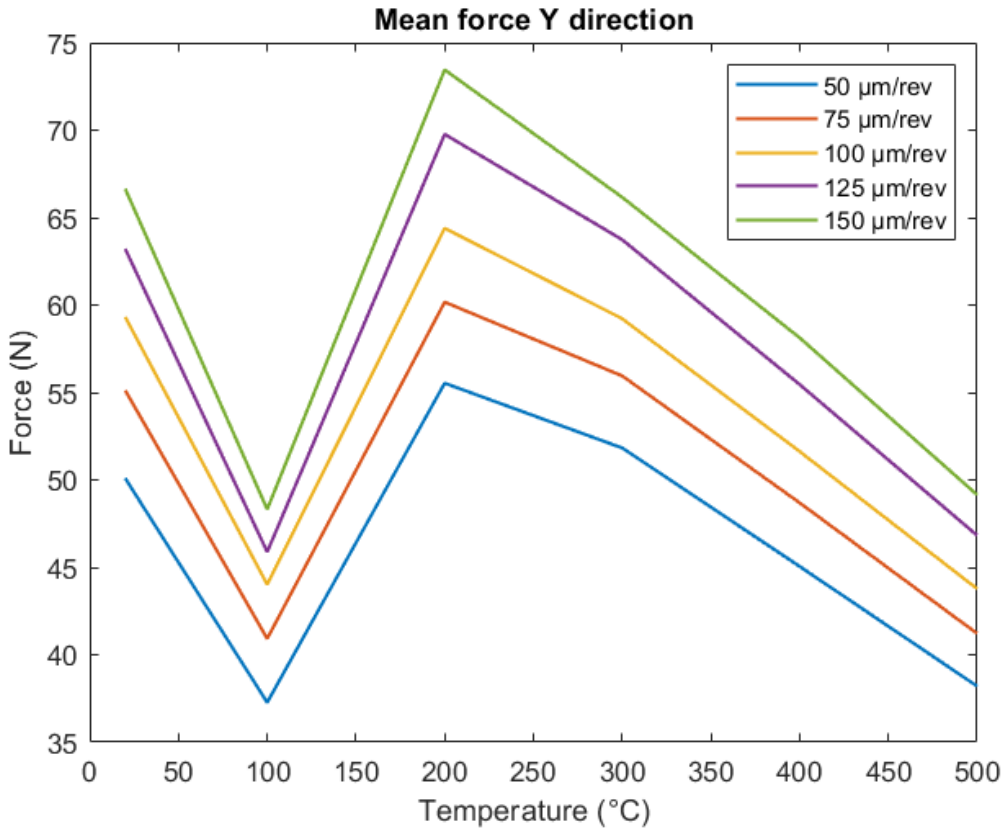


Figure 4.16: Mean force in Y over a range of temperatures and feed rates in Ti-6Al-4V.

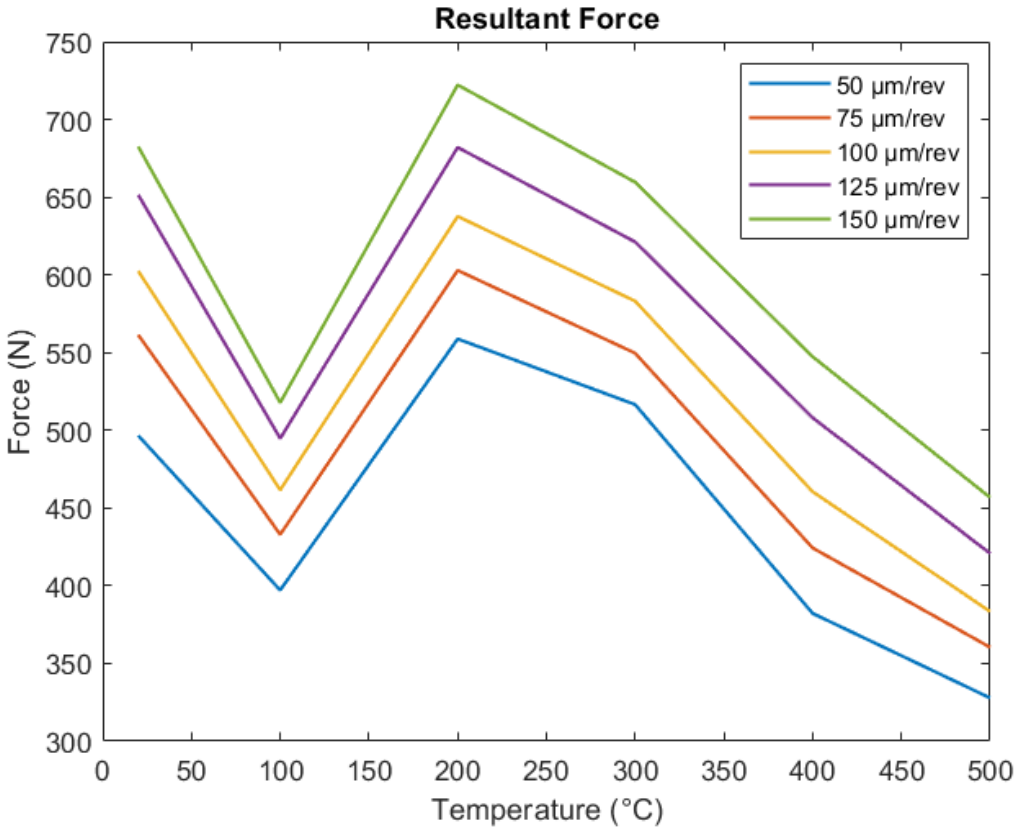


Figure 4.17: Peak resultant force over a range of temperatures and feed rates in Ti-6Al-4V.

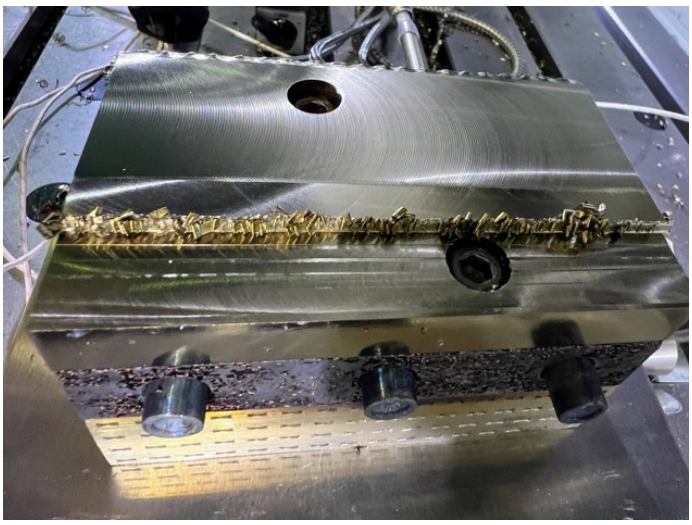


Figure 4.18: Chip welding at 500°C, conventional milling.

4.3 Milling time domain simulation

The four coefficients for the cutting force model were determined for each temperature by linear regression using the average of the measured cutting forces over a range of feed rates. The k_t and k_n terms are linearly dependent with the chip thickness. The k_{te} and k_{ne} coefficients are independent of chip thickness and represent rubbing or plowing [13]. The mean force in the x and y directions as a function of the four cutting force coefficients is given in Equation 4.2.

$$\begin{aligned} F_n &= k_n b h + k_{ne} b \\ F_t &= k_t b h + k_{te} b \end{aligned} \tag{4.1}$$

Where F_n = normal force component, F_t = tangential force component

$$\begin{aligned} \overline{F}_x &= \left[\frac{N_t b f_t}{8\pi}(-k_t \cos(2\phi) + k_n(2\phi - \sin(2\phi))) + \frac{N_t b}{2\pi}(k_{te} \sin\phi + k_{ne} \cos\phi) \right]_{\phi_s}^{\phi_e} \\ \overline{F}_y &= \left[\frac{N_t b f_t}{8\pi}(k_n \cos 2\phi + k_t(2\phi - \sin(2\phi))) + \frac{N_t}{2\pi}(k_{te} \cos\phi + k_{ne} \sin\phi) \right]_{\phi_s}^{\phi_e} \end{aligned} \tag{4.2}$$

The start and exit angles for down/climb milling are defined in Equation 4.3.

$$\begin{aligned} \phi_s &= \pi - \cos^{-1}\left(\frac{r-a}{r}\right) \\ \phi_s &= \pi \end{aligned} \tag{4.3}$$

Let:

$$\begin{aligned} cs_1 &= cos(\phi_e) - cos(\phi_s) \\ cs_2 &= cos(2\phi_e) - cos(2\phi_s) \\ sn_1 &= sin(\phi_e) - sin(\phi_s) \\ sn_2 &= sin(2\phi_e) - sin(2\phi_s) \\ df_2 &= 2\phi_e - 2\phi_s \\ c_1 &= \frac{N_t b}{2\pi} \\ c_3 &= \frac{N_t b}{8\pi} \end{aligned} \tag{4.4}$$

For simplified force equations:

$$\overline{F}_x = f_t c_3[-k_t cs_2 + k_n df_2 - k_n sn_2] + c_2[k_{te} sn_1 - k_{ne} cs_1] \tag{4.5}$$

$$\overline{F}_y = f_t c_3[k_t df_2 - k_t sn_2 + k_n cs_2] - c_2[k_{te} cs_1 + k_{ne} sn_1] \tag{4.6}$$

Equations 4.5 and 4.6 are in slope-intercept form, $\overline{F} = a_0 + a_1 f_t$, where:

$$\begin{aligned} a_{1x} &= c_3[-k_t cs_2 + k_n(df_2 - sn_2)] \\ a_{1y} &= c_3[k_t(df_2 - sn_2) + k_n cs_2] \\ a_{0x} &= c_1[k_{te} sn_1 - k_{ne} cs_1] \\ a_{0y} &= -c_1[k_{te} cs_1 + k_{ne} sn_1] \end{aligned} \tag{4.7}$$

Rewriting in matrix form gives:

$$\begin{aligned} \begin{bmatrix} a_{0x} \\ a_{0y} \end{bmatrix} &= \begin{bmatrix} c_1 sn_1 & -c_1 cs_1 \\ -c_1 cs_1 & -c_1 sn_1 \end{bmatrix} \begin{Bmatrix} k_{te} \\ k_{ne} \end{Bmatrix} \\ \begin{bmatrix} a_{1x} \\ a_{1y} \end{bmatrix} &= \begin{bmatrix} -c_3 cs_2 & c_3(df_2 - sn_2) \\ c_3(df_2 sn_2) & c_3 cs_2 \end{bmatrix} \begin{Bmatrix} k_t \\ k_n \end{Bmatrix} \end{aligned} \tag{4.8}$$

Solving for k_t,k_n,k_{te},k_{ne}:

$$\begin{Bmatrix} k_t \\ k_n \end{Bmatrix} = \begin{bmatrix} -c_3 cs_2 & c_3(df_2 - sn_2) \\ c_3(df_2 sn_2) & c_3 cs_2 \end{bmatrix}^{-1} \begin{bmatrix} a_{1x} \\ a_{1y} \end{bmatrix} \tag{4.9}$$

$$\begin{Bmatrix} k_{te} \\ k_{ne} \end{Bmatrix} = \begin{bmatrix} c_1 sn_1 & -c_1 cs_1 \\ -c_1 cs_1 & -c_1 sn_1 \end{bmatrix}^{-1} \begin{bmatrix} a_{0x} \\ a_{0y} \end{bmatrix} \tag{4.10}$$

Solving for the cutting force coefficients:

$$k_t = \frac{c_3}{c_4} cs_2 a_{1x} - \frac{c_3}{c_4}(df_2 - sn_2) a_{1y} \tag{4.11}$$

$$k_n = \frac{-c_3}{c_4}(df_2 - sn_2) a_{1x} - \frac{c_3}{c_4} cs_2 a_{1y} \tag{4.12}$$

$$k_{te} = \frac{-c_1}{c_2} sn_1 a_{0x} + \frac{c_1}{c_2} cs_1 a_{oy} \tag{4.13}$$

$$k_{ne} = \frac{c_1}{c_2} cs_1 a_{0x} + \frac{c_1}{c_2} sn_1 a_{0y} \tag{4.14}$$

Equations 4.11 to 4.3 are valid for any arbitrary start and exit angles.

The linear fit between cutting force and feed rate for all temperatures are shown in Figures 4.19 and 4.20. The slope and intercept from the fits were used to calculate the set of cutting force coefficients for each temperature, shown in Table 4.7 and Figure 4.21. As expected, the coefficients follow the trend seen in the measured force data. The temperature dependent coefficients were used in the time domain milling simulation to calculate cutting force. The average peak forces for the Y direction are presented in Table 4.8. Figures 4.22, 4.23, 4.24, and 4.25 show good agreement between the measured and modeled forces at 20°C and 500°C respectively.

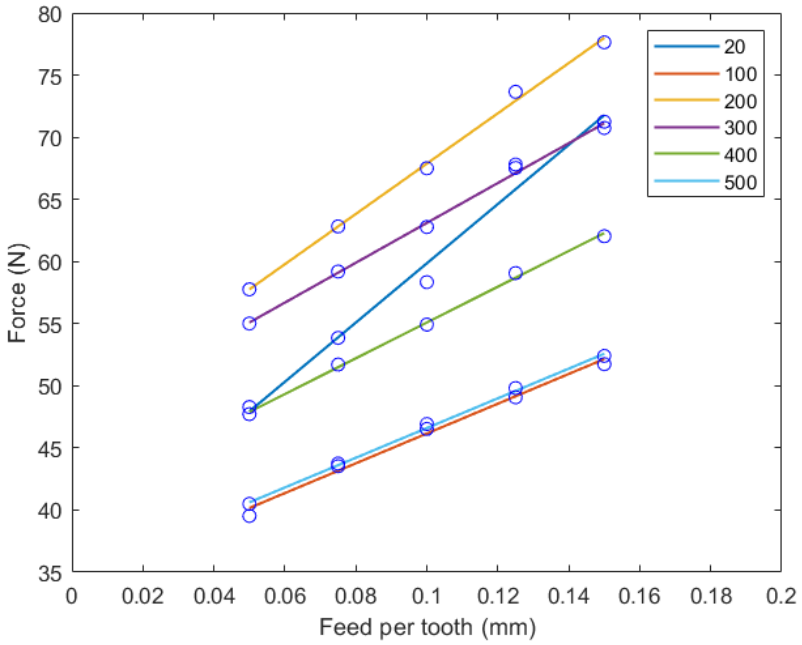


Figure 4.19: Linear fit of cutting force vs. feed rate for Y direction over all temperatures.

Table 4.7: Cutting force coefficients with temperature.

Temperature (°C)	K_t (N/mm^2)	K_n (N/mm^2)	K_{te} (N/mm)	K_{ne} (N/mm)
20	1729.0	1094.7	15.1	131.7
100	1152.8	352.7	13.6	125.3
200	1752.1	730.7	21.8	173.2
300	1505.4	497.1	24.7	169.6
400	1209.7	545.5	54.3	130.2
500	1079.9	400.6	40.7	113.5

Table 4.8: Simulated average of the Y peak cutting force.

	Temperature (°C)					
	20	100	200	300	400	500
Feed Rate (µm)	Cutting force (N)					
50	344.5	272.1	397.1	374.6	344.6	288.6
75	421.6	306.0	458.7	420.3	393.5	329.8
100	501.2	349.0	529.9	477.3	444.0	372.8
125	580.9	393.1	601.7	535.8	494.5	415.8
150	660.6	437.3	673.4	594.3	545.0	458.8

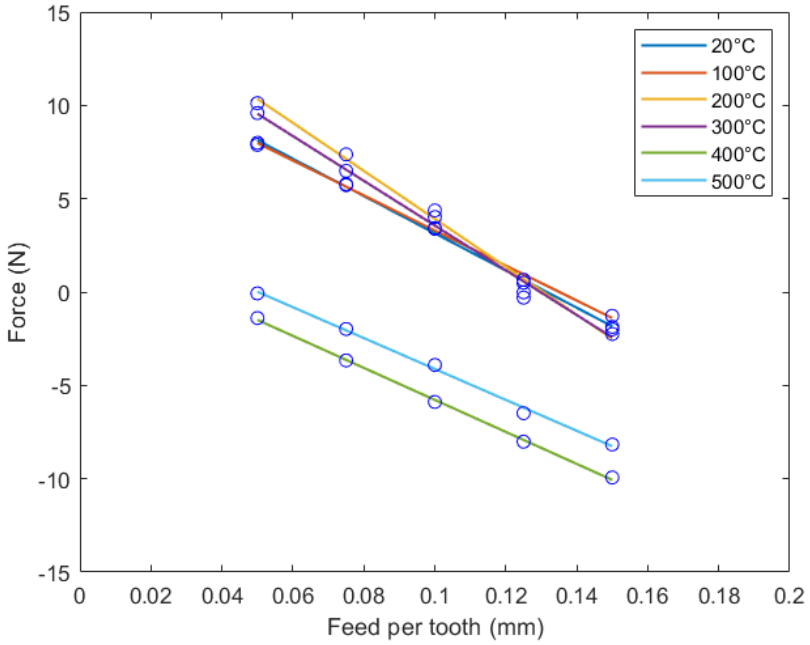


Figure 4.20: Linear fit of cutting force vs. feed rate for X direction directions over all temperatures.

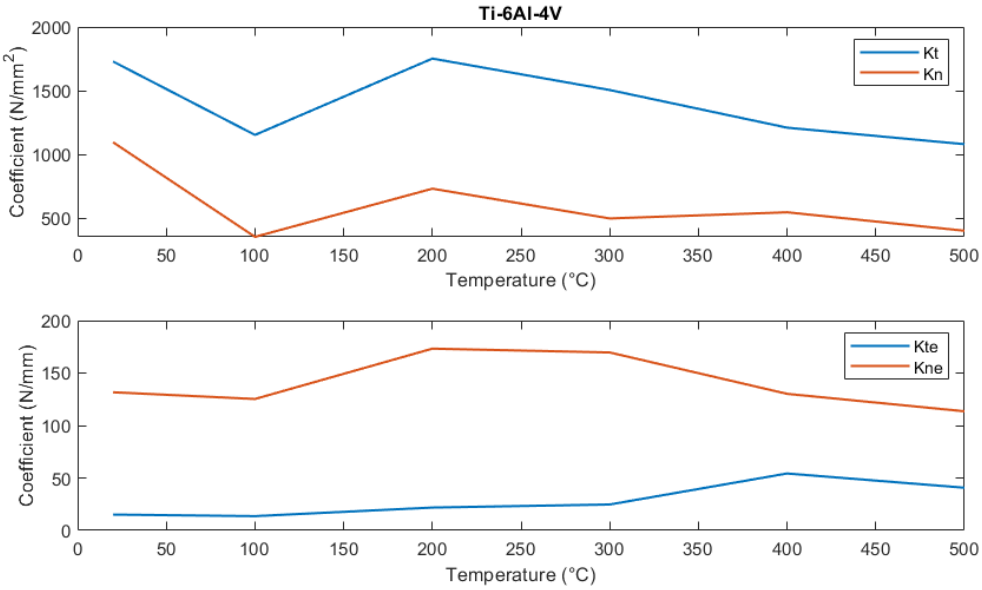


Figure 4.21: Cutting for coefficients with temperature.

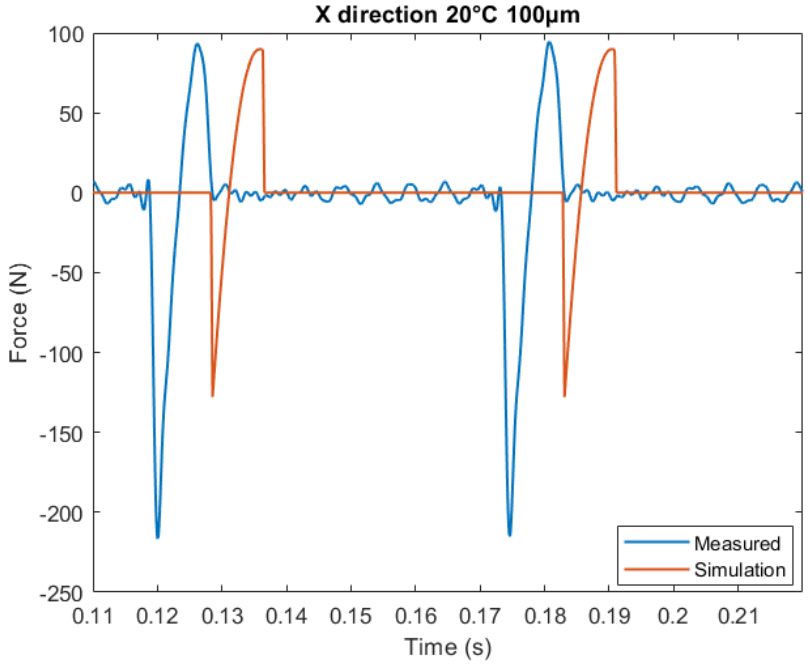


Figure 4.22: Measured and simulated X force at 20°C and 100$\frac{\mu m}{tooth}$.

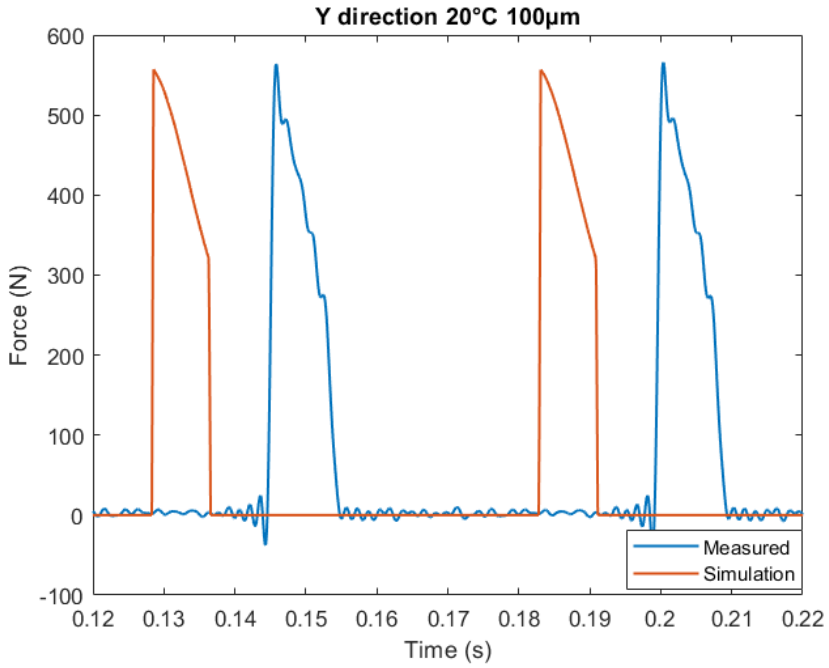


Figure 4.23: Measured and simulated Y force at 20°C and $100\frac{\mu m}{tooth}$.

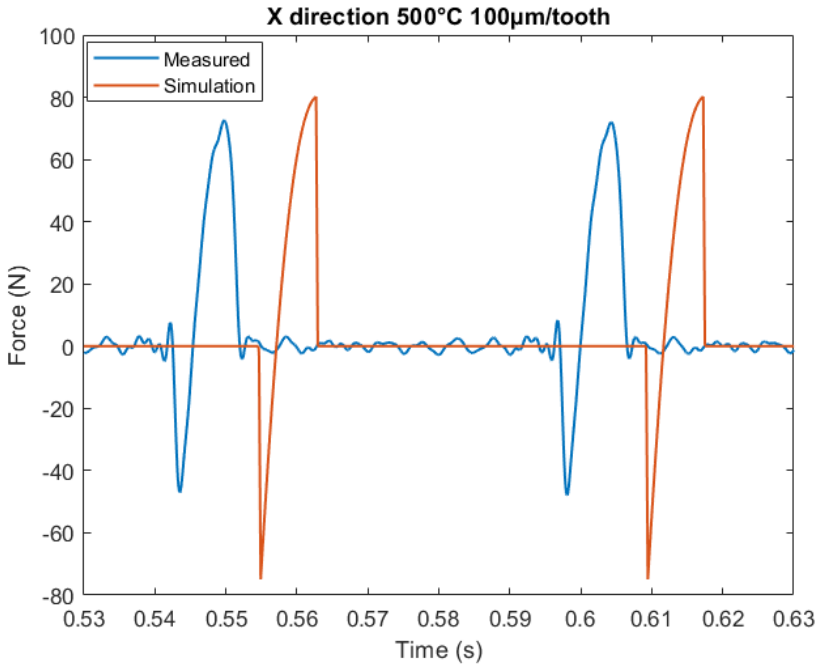


Figure 4.24: Measured and simulated X force at 500°C and $100\frac{\mu m}{tooth}$.

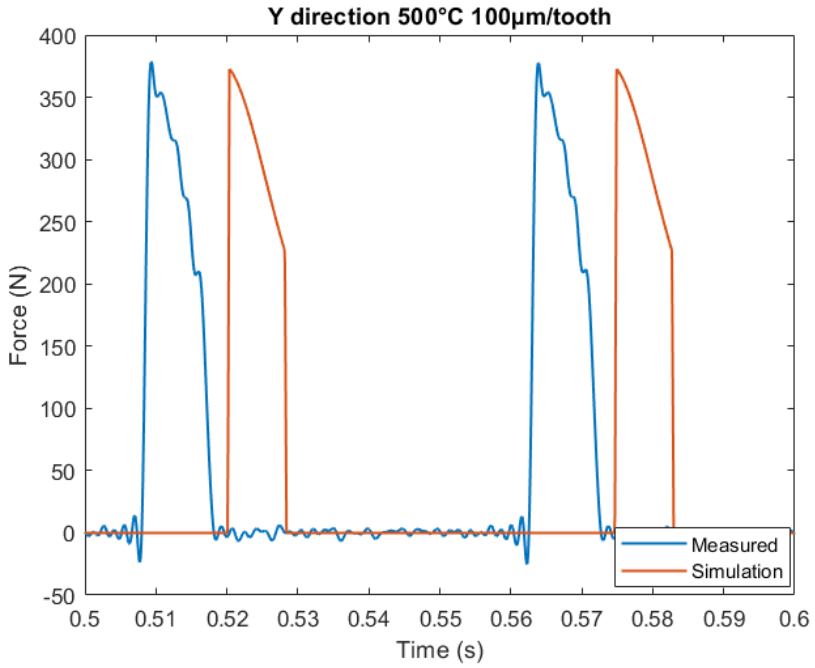


Figure 4.25: Measured and simulated Y force at 500°C and $100\frac{\mu m}{tooth}$.

Chapter 5

Conclusion

Cutting force coefficients, workpiece dynamics, and uncut chip area all change as a function of temperature. In a traditional milling process, these parameters are nearly constant. The bulk workpiece temperature remains well below the working limit of the material, generally near room temperature. To accurately measure temperature dependent cutting force, an elevated temperature cutting force dynamometer was designed, constructed, and tested.

A workpiece surface temperature uncertainty of $\pm 10.27°C$ at $500°C$ was achieved using a combination of N type thermocouples, constant conditions, and IR thermography, an 80% improvement over the use of IR thermography in traditional TEM. A novel high stiffness thermal insulator was designed, manufactured, and tested that used lattice structures to geometrically increase the thermal resistance and additive manufacturing to decrease the thermal conductivity of the base material. The thermal protection system developed using a combination of the high stiffness insulator, convective cooling, and a glass-silicon composite, reduced the temperature from over $1000°C$ at the heating element to less than $60°C$ at the dynamometer platform. As a result the change in natural frequency and stiffness with workpiece temperature was limited to 2.5% and 4.5% respectively. A modest change in temperature, $40°C$, yielded a relatively large change in stiffness.

Ti-6Al-4V cutting forces were measured for five feed rates, {50, 75, 100, 125 and 150}$\frac{\mu m}{tooth}$, and six nominal temperatures, {20, 100, 200, 300, 400, 500}°C. A process was developed to limit the effect of thermal expansion on uncut chip thickness. Without accounting for the change in workpiece geometry due to thermal expansion, the axial depth would have increased 25% at 500°C. A maximum decrease in cutting force of 53% from room temperature to 500°C was measured. Surprisingly, an average 20% reduction in cutting force at 100°C and an average 11% increase in cutting force at 200°C, when compared to room temperature, was measured.

The results presented in this dissertation show that traditional milling models and assumptions are insufficient for a hybrid process. Developing an elevated temperature cutting force dynamometer enabled the measurement of cutting forces at constant elevated temperatures and the fitting of temperature dependent cutting force coefficients. The coefficients introduced temperature dependence to a time domain milling simulation that showed good agreement between the measured and simulated cutting forces.

Hybrid manufacturing is a relatively new process that leverages the best aspects of additive and traditional subtractive manufacturing to enable the production of a new class of parts. The development of process models is critical to realizing the potential of hybrid manufacturing. The elevated temperature dynamometer and updated milling force model enable better stability prediction and process parameter selection. Parameters on the additive side can be chosen to keep a part in an optimal temperature range for milling, additive preforms can be designed with stiffness to match the anticipated cutting forces, allowing for higher metal removal rates, and milling parameters can be chosen that result in stable conditions over the anticipated part temperatures. The result is improved part quality, reduced cycle time, and wider industry adoption.

Future Work

The hybrid manufacturing process requires more research to capture the spatial and temporal variability. The effect of temperature on the natural frequency and stiffness of representative part geometries should be investigated. Models to predict the thermal growth and distortions and compensate for them in the milling tool path are critical to producing hybrid components in the methods described in this study.

References

[1] U.S. Department of Energy. Doe quadrennial technology review 2015: Technology assessment on addtive manufacturing. *Quadrennial Technology Review*, page 36, 2015.

[2] Wohlers Associates. *Wohlers reports on record AM growth*, volume 74. Wohlers, 2019.

[3] VW Group Porsche. 3d printing technology optimises pistons for the powerful 911 gt2 rs.

[4] Sandvik-Coromant. Lightweight coromill® 390 produced using additive manufacturing reduces vibration in long-overhang milling.

[5] Phillip Keane. Boeing tests 3d printing for apache helicopter parts.

[6] Tiago A. Rodrigues, V. Duarte, Julian A. Avila, Telmo G. Santos, R. M. Miranda, and J. P. Oliveira. Wire and arc additive manufacturing of hsla steel: Effect of thermal cycles on microstructure and mechanical properties. *Additive Manufacturing*, 27(February):440–450, 2019.

[7] Sung Ho Moon and Choon Man Lee. A study on the machining characteristics using plasma assisted machining of aisi 1045 steel and inconel 718. *International Journal of Mechanical Sciences*, 142–143(April):595–602, 2018.

[8] J Tlusty and M Polacek. Besipiele der behandlung der selbsterregten schwingungder werkzeugmaschinen. 1957.

[9] J. Tlusty and M. Polaceck. The stability of machine tools against self-excited vibrations in machining. *International Research in Production Engineering*, 1963.

[10] S.A. Tobias and W. Fishwick. Theory of regenerative machine tool chatter. *The Engineer*, 1958.

[11] H. Merrit. Theory of self-excited machine tool chatter. *Journal of Engineering for Industry*, 1965.

[12] George Tlusty. *Manufacturing process and equipment*. Pearson, 1999.

[13] Tony Schmitz and K. Scott Smith. *Machining Dynamics*. Springer, 2016.

[14] S. Smith and J. Tlusty. An overview of modeling and simulation of the milling process. *Journal of Engineering for Industry*, 113:169–175, May 1991.

[15] Yusuf Altintas, Gabor Stepan, Erhan Budak, Tony Schmitz, and Zekai Murat Kilic. Chatter stability of machining operations. *Journal of Manufacturing Science and Engineering, Transactions of the ASME*, 142(11), 2020.

[16] Tony L. Schmitz and Matt A. Davies. Improving high-speed machining material removal rates by rapid dynamic analysis. *CIRP Annals - Manufacturing Technology*, 50, 2001.

[17] Tony L. Schmitz. Chatter recognition by a statistical evaluation of the synchronously sampled audio signal [2]. *Journal of Sound and Vibration*, 262(3):721–730, 2003.

[18] S. Sun, M. Brandt, and M. S. Dargusch. Thermally enhanced machining of hard-to-machine materials - a review. *International Journal of Machine Tools and Manufacture*, 50(8):663–680, 2010.

[19] Tosu, Nihat, Ozler, and Latif. A study of tool life in hot machining using artificial neural networks and regression analysis method. *Journal of Materials Processing Technology*, 124:99–104, 2002.

[20] Jie Luo, Hongtao Ding, and Albert Shih. Induction-heated tool machining of elastomers - part 2: Chip morphology, cutting forces, and machined surfaces. *Machining Science and Technology*, 9(4):567–588, 2005.

[21] Turnad L. Ginta, A. K.M.Nurul Amin, Mohd Amri Lajis, A. N.Mustafizul Karim, and H. C.D.Mohd Radzi. Improved tool life in end milling ti-6al-4v through workpiece preheating. *European Journal of Scientific Research*, 27(3):384–391, 2009.

[22] Maher Baili, Vincent Wagner, Gilles Dessein, Julien Sallaberry, and Daniel Lallement. An experimental investigation of hot machining with induction to improve ti-5553 machinability. *Applied Mechanics and Materials*, 62:67–76, 2011.

[23] L. N. López De Lacalle, J. A. Sánchez, A. Lamikiz, and A. Celaya. Plasma assisted milling of heat-resistant superalloys. *Journal of Manufacturing Science and Engineering, Transactions of the ASME*, 126(2):274–285, 2004.

[24] G. Madhavulu and Basheer Ahmed. Hot machining process for improved metal removal rates in turning operations. *Journal of Materials Processing Tech.*, 44(3–4):199–206, 1994.

[25] Zhipeng Pan, Yixuan Feng, Yu Ting Lu, Yu Fu Lin, Tsung Pin Hung, Fu Chuan Hsu, and Steven Y. Liang. Force modeling of inconel 718 laser-assisted end milling under recrystallization effects. *International Journal of Advanced Manufacturing Technology*, 92(5–8):2965–2974, 2017.

[26] Mark Anderson, Rahul Patwa, and Yung C. Shin. Laser-assisted machining of inconel 718 with an economic analysis. *International Journal of Machine Tools and Manufacture*, 46(14):1879–1891, 2006.

[27] M. W. Norazlan, Z. Mohid, and E. A. Rahim. Laser assisted machining of titanium alloys. *Materials Science Forum*, 763(July):91–106, 2013.

[28] Jinn-Fa Wu and Yeou-Bin Guu. Cutting metal by electricity, 2006.

[29] Christian Brecher, Michael Emonts, Chris Jörg Rosen, and Jan Patrick Hermani. Laser-assisted milling of advanced materials. *Physics Procedia*, 12(PART 1):599–606, 2011.

[30] Center for laser based manufacturing, 2016.

[31] Gary Kent Hedberg. Laser assisted milling of difficult to machine materials. Master's thesis, Purdue, 2013.

[32] Asit Kumar Parida. Analysis of chip geometry in hot machining of inconel 718 alloy. *Iranian Journal of Science and Technology - Transactions of Mechanical Engineering*, 43(s1):155–164, 2019.

[33] Balkrishna Rao, Chinmaya R. Dandekar, and Yung C. Shin. An experimental and numerical study on the face milling of ti-6al-4v alloy: Tool performance and surface integrity. *Journal of Materials Processing Technology*, 211(2):294–304, 2011.

[34] M Davami and M Zadshakoyan. Investigation of tool temperature and surface quality in hot machining of hard-to-cut materials. *International Journal of Materials and Metallurgical Engineering*, 2(10):240–244, 2008.

[35] Hassan Zamani, Jan Patrick Hermani, Bernhard Sonderegger, and Christof Sommitsch. 3d simulation and process optimization of laser assisted milling of ti6al4v. *Procedia CIRP*, 8:75–80, 2013.

[36] Yao Xi, Michael Bermingham, Gui Wang, and Matthew Dargusch. Sph/fe modeling of cutting force and chip formation during thermally assisted machining of ti6al4v alloy. *Computational Materials Science*, 84:188–197, 2014.

[37] Carl E. Leshock, Jin Nam Kim, and Yung C. Shin. Plasma enhanced machining of inconel 718: Modeling of workpiece temperature with plasma heating and experimental results. *International Journal of Machine Tools and Manufacture*, 41(6):877–897, 2001.

[38] Asit Kumar Parida and Kalipada Maity. Experimental investigation on tool life and chip morphology in hot machining of monel-400. *Engineering Science and Technology, an International Journal*, 21(3):371–379, Jun 2018.

[39] Turnad L Ginta and A K M Nurul Amin. Force and tool life models in end milling titanium alloy ti-4al-4v with thermally-assisted machining. *Material Science*, 1(1):1–5, 2012.

[40] Robert Wiedenmann and Michael F. Zaeh. Laser-assisted milling-process modeling and experimental validation. *CIRP Journal of Manufacturing Science and Technology*, 8:70–77, 2015.

[41] R. A. Rahman Rashid, S. Sun, G. Wang, and M. S. Dargusch. An investigation of cutting forces and cutting temperatures during laser-assisted machining of the ti-6cr-5mo-5v-4al beta titanium alloy. *International Journal of Machine Tools and Manufacture*, 63:58–69, 2012.

[42] A. K.M.N. Amin and M. Abdelgadir. The effect of preheating of work material on chatter during end milling of medium carbon steel performed on a vertical machining center (vmc). *Journal of Manufacturing Science and Engineering, Transactions of the ASME*, 125(4):674–680, 2003.

[43] E. Uhlmann and P. Rasper. Influences on specific cutting forces and their impact on the stability behaviour of milling processes. *Production Engineering*, 5(2):175–181, 2011.

[44] Dongqing Yang, Gang Wang, and Guangjun Zhang. Thermal analysis for single-pass multi-layer gmaw based additive manufacturing using infrared thermography. *Journal of Materials Processing Technology*, 244:215–224, 2017.

[45] Bintao Wu, Donghong Ding, Zengxi Pan, Dominic Cuiuri, Huijun Li, Jian Han, and Zhenyu Fei. Effects of heat accumulation on the arc characteristics and metal transfer behavior in wire arc additive manufacturing of ti6al4v. *Journal of Materials Processing Technology*, 250(July):304–312, 2017.

[46] D.A. Swyt. Uncertainties in dimensional measurements made at nonstandard temperatures. *Journal of Research of the National Institute of Standards and Technology*, 99(1):31, January 1994.

[47] M.F. Zaeh, R. Wiedenmann, and R. Daub. A thermal simulation model for laser-assisted milling. *Physics Procedia*, 5:353–362, 2010.

[48] B Lane, E Whitenton, V Madhavan, and A Donmez. Uncertainty of temperature measurements by infrared thermography for metal cutting applications. *Metrologia*, 50(6):637–653, December 2013.

[49] Kistler Group. *Multicomponent Dynamometer*.

[50] Michael Gomez and Tony Schmitz. Low-cost, constrained-motion dynamometer for milling force measurement. *Manufacturing Letters*, 25:34–39, 2020.

[51] Michael F. Gomez and Tony L. Schmitz. Displacement-based dynamometer for milling force measurement. *Procedia Manufacturing*, 34:867–875, 2019.

[52] American Iron and Steel Institute. *High-temperature characteristics of stainless stee*.

[53] Krister Dovstam, Peter Göransson, and Otto Gartmeier. On linear modeling of interface damping in vibrating structures. *Journal of Sound and Vibration*, 331(19):4299–4312, September 2012.

[54] Xuan Luo Yogng Yi Fang Yang Hao Ma, Xiaoyang Zheng. Simulation and analysis of mechanical properties of silica aerogels: From rationalization to prediction.

[55] N. Burger, A. Laachachi, M. Ferriol, M. Lutz, V. Toniazzo, and D. Ruch. Review of thermal conductivity in composites: Mechanisms, parameters and theory. 61:1–28.

[56] A286 bolts.

[57] Alloy Center. Titanium alloy grade 5 /ti-6al-4v, 2015.

[58] M.J. Bermingham, S. Palanisamy, and M.S. Dargusch. Understanding the tool wear mechanism during thermally assisted machining Ti-6Al-4V. *International Journal of Machine Tools and Manufacture*, 62:76–87, November 2012.

[59] Omega. Ansi thermocouple tolerances.

[60] Teledyne FLIR. Flir a50/a70 datasheet.

[61] J. Agapiou and Stephenson D. Cutting tool wear and failure mechanisms.

[62] M.A. Davies, T. Ueda, R. M'Saoubi, B. Mullany, and A.L. Cooke. On The Measurement of Temperature in Material Removal Processes. *CIRP Annals*, 56(2):581–604, 2007.

[63] I. Arriola, E. Whitenton, J. Heigel, and P.J. Arrazola. Relationship between machinability index and in-process parameters during orthogonal cutting of steels. *CIRP Annals*, 60(1):93–96, 2011.

Vita

Justin West completed his bachelor's degree in mechanical degree at the University of Florida in 2017 and master's degree at the University of Tennessee in 2022. He has worked as research staff member in the Intelligent Machine Tools Group at Oak Ridge National Laboratory since 2019.